REVIEW

Imaging in translational cancer research

Felix T. Kurz, Heinz-Peter Schlemmer

Department of Radiology, German Cancer Research Center, Heidelberg 69120, Germany

ABSTRACT   This review is aimed at presenting some of the recent developments in translational cancer imaging research, with a focus on novel, recently established, or soon to be established cross-sectional imaging techniques for computed tomography (CT), magnetic resonance imaging (MRI), and positron-emission tomography (PET) imaging, including computational investigations based on machine-learning techniques.

KEYWORDS   Cancer imaging; computed tomography (CT); magnetic resonance imaging (MRI); positron emission tomography (PET); cross-sectional imaging

Introduction

For preclinical and clinical research and subsequent translation to routine applications in patient care, such as the development of novel targeted therapies for metastatic disease, diagnostic imaging has a pivotal role in disease detection, grading, treatment planning, therapy monitoring, and detection of recurrence[1]. With the availability of ever more powerful computational methods, new imaging biomarkers may emerge and shape future clinical decision-making tools, and may also be used in fundamental and translational research[2]. The current arsenal of tomographic imaging techniques is continually being updated and improved upon, thus leading to the development and establishment of new computed tomography (CT) techniques with improved contrast, and spatial and temporal resolution, as well as diminished radiation exposure[3]; novel imaging sequences in magnetic resonance imaging (MRI) for assessing, e.g., the specific microstructural composition of biological tissue *via* its diffusive properties[4]; new molecular markers to advance positron-emission tomography (PET) imaging[5,6]; improved hybrid imaging techniques combining PET and CT or MRI[7,8]; and novel imaging-sifting computational methods based on machine-learning and high-throughput analysis of large patient cohorts[9,10].

Although many techniques may offer promising applications, their potential to be translated to routine clinical imaging is continually being evaluated or reconsidered, and translation is not ensured; some techniques, such as MRI spectroscopy, have been well-known for several decades but remain rarely used in routine imaging[11]. However, the role of MRI spectroscopy in oncological research is indispensable and may increase, on the basis of sequences with improved artifact reduction, resolution, and time efficacy[12].

Typically, the interpretation of *in vivo* tomographic imaging in preclinical settings is compared with results from *ex vivo* histology and/or microscopy images with much better spatial resolution, as well as with patient characteristics, to obtain integrative correlative measures that may indicate disease status. On the basis of these results, the interpretation is extended to clinical imaging and serves as a basis for clinical decision-making. Animal studies may even be used to enable correlative approaches that compare *in vivo* tomographic imaging with *in vivo* microscopic imaging from, e.g., multiphoton microscopy[13]. These experimental imaging procedures are becoming increasingly important because they allow for the application and direct comparison of common clinical imaging techniques with ground truth microscopic images in a non-destructive *in vivo* setting, thus providing the benefit of a live view of functional disease properties otherwise not possible in human imaging.

CT imaging

CT imaging is currently the most commonly used cross-sectional imaging method in radiological imaging, and is applied in emergency situations, screening protocols, and cancer

Correspondence to: Felix T. Kurz and Heinz-Peter Schlemmer
E-mail: f.kurz@dkfz.de and h.schlemmer@dkfz.de

staging examinations. In fact, most oncological staging procedures, particularly in thoracic and abdominal radiology, rely on standardized CT imaging protocols according to national consensus guidelines such as those from the association of the scientific medical societies in Germany (AWMF). CT imaging is rapid and allows for quantitative evaluation of neoplastic disease; however, it has the drawbacks of radiation exposure through X-rays and contraindication for patients with allergies to CT contrast agents and/or who are at risk of iodinated contrast-induced thyrotoxicosis or impaired renal function.

Beyond improving imaging resolution and speed, novel techniques in CT imaging have been aimed at decreasing radiation exposure and the need for contrast agent. Nonetheless, currently available commercial CTs are already approaching their physical limits in terms of technological advances in gantry, tube, and detector design[14]. The number of detector rows in the z-direction (along the patient long axis) is typically between 192 and 320; this number, together with the maximum detector panel width of 16 cm, is not expected to substantially increase in the coming years, because it already allows for adequate cardiac imaging within one heartbeat[15]. One recently established technique is CT-based measurement of the fractional flow reserve to model flow in coronary arteries by using anatomic physiological modeling, that can be used to quantify the extent of coronary artery disease, which is a potential radiation-therapy related side effect[16,17].

Advances in tube technology saw the introduction of specific prefilters that selectively remove photons with low energy from the photon spectrum of the CT cone beam, thus decreasing radiation exposure and enabling faster scanning[18,19]. These advances allow for high-speed, low-kilovolt (kV) examinations that can accommodate patients with high body-mass index, and 100 kV has replaced 120 kV as the new imaging standard[20-22]. The decrease in radiation exposure is highly sought after for future screening exams. To date, low-dose CT screening is advised only for lung cancer screening in adults 50–80 years of age with a history of smoking of at least 20 pack years[23], and remains under investigation for the detection of early lung cancer[24].

Photon counting detector CT imaging

Developments in CT detectors have included the introduction of smaller detector elements as well as so-called photon counting detectors (**Figure 1**). In a conventional, energy-integrating detector, X-rays enter a solid-state scintillator detector, thus generating scintillation light through interaction, which hits a photodiode that converts the light into an electrical signal proportional to the sum of all detected X-ray photon energies, regardless of the individual photon energies[25]. In photon counting detectors (PCDs), however, the interaction of X-ray photons with the single layer semiconductor detector material (typically cadmium zinc telluride) produces positive and negative charges, wherein the negative charges are drawn to pixelated anodes and record individual X-ray photons, thus enabling direct conversion to an electronic signal proportional to the photons' individual energies[26]. Because the signal is recorded within only nanoseconds, detector pixel sizes can be designed to enable photon energy discrimination in clinical CT imaging[27]. Measuring individual photon energies has high potential to be adapted by using elements such as bismuth, gadolinium, and iodine to produce new imaging contrasts and potentially enable multi-phase imaging within a single recording[28,29].

The following contrasts are currently being investigated. PCDs in micro-CT imaging have been used in nanoparticle contrast agent imaging of mouse sarcoma with iodine and gadolinium nanoparticles, thus achieving improved visualization of the tumor vasculature and intratumoral distribution patterns of contrast agent nanoparticles[30]. In a similar study, iodine and gadolinium based intravenous contrast agent injections in rats have been demonstrated to feasibly differentiate peritoneal metastases in colorectal carcinoma with a specificity of 100%[31]. Furthermore, in a mouse model of soft tissue sarcoma receiving radiation therapy, the radiomic features from PCD CT with iodine contrast have been found to be superior to those of conventional micro-CT in differentiating among various tumor metrics[32]. Such functional characterizations of tumor tissue are expected to be important in future preclinical research and may be used in whole-body PCD CT imaging for translational research from rodents to humans[33].

Owing to the smaller pixel sizes, the in-plane resolution and longitudinal spatial resolution are significantly better in PCD CT scanners than conventional CT scanners, and in-plane resolutions as high as 50–150 μm have been achieved[34,35]. This improvement enables better detection of small structures in biological tissue such as small bronchi[36]. Moreover, ultra-high-resolution PCD CT imaging has shown potential in detecting small osteolytic bone metastases in breast cancer that would have otherwise been missed by conventional imaging[37]. In addition, the improved resolution also allows for the
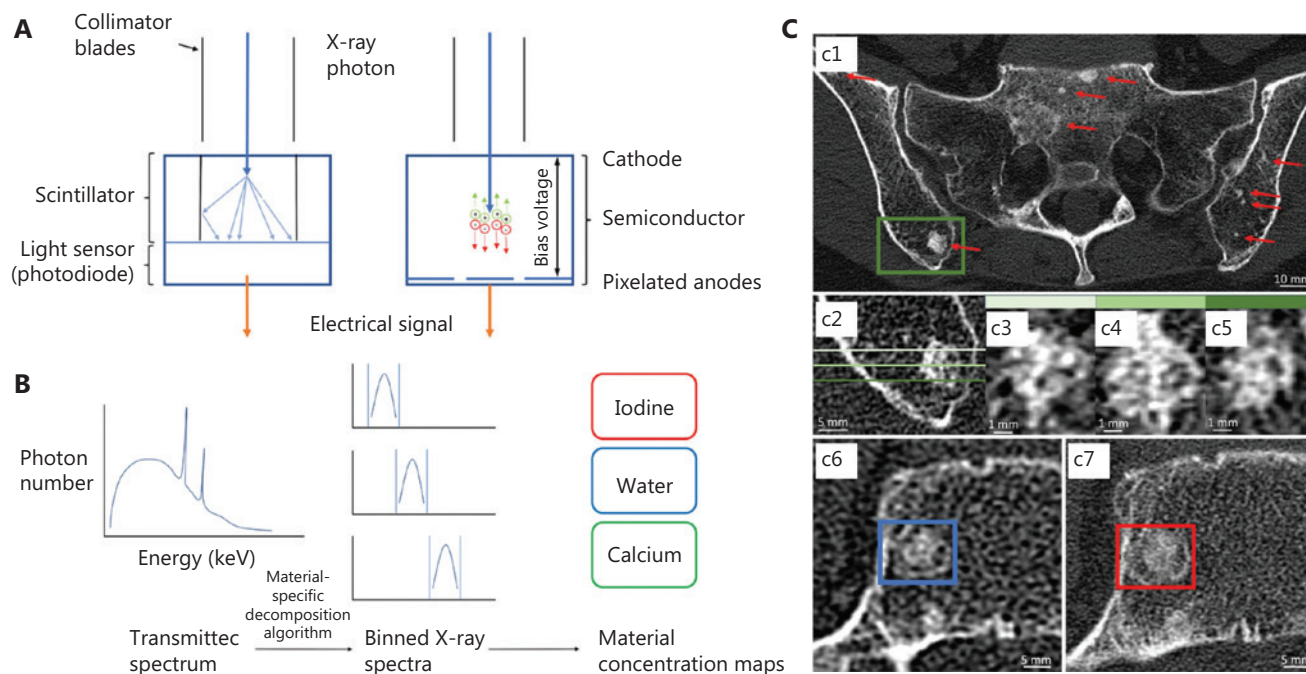
Figure 1 (A) Schematic representation of the integrated energy detector (EID; left panel) and the photon-counting detector (PCD; right panel). In the EID, X-rays enter a solid-state scintillator detector and convert to scintillation light through interaction. The resulting photons hit a photodiode, which converts the light to an electrical signal proportional to the sum of all X-ray photon energies. The PCD allows X-ray photons to interact with a semiconductor material layer, thus producing positive and negative charges. The negative charges are drawn to pixelated anodes and record individual X-ray photons directly in an electrical signal proportional to the photons' individual energy. (B) The PCD allows for recording of different energy spectra by using energy thresholds (middle panel) that produce material-specific maps in a manner dependent on the material concentration within the tissue (for instance, iodine, water, calcium), on the basis of specific material decomposition algorithms. (C) Unenhanced EID (c6) and PCD (c1–c5, c7) images of a 68-year-old patient with unifocal medium-grade breast cancer and histologically confirmed osseous metastases (CT window: C = 500 HU, W = 1,500 HU). (c1) Red arrows indicate multiple osteoblastic metastases with one metastasis in the right iliac bone with a complex sclerotic composition pattern (c2–c5). (c6, c7) EID and PCD CT image of a metastasis in the right fifth lumbar vertebra. The gain in resolution and therefore diagnostic accuracy is clearly seen. Figures in (A, B) are adapted from Ref.[26] (CC BY 4.0 license), and the images in (C) are adapted from Figure 3 in Ref.[37] (CC BY 4.0 license).

detection of microcalcifications in breast cancer specimens with sensitivity and specificity comparable to those of digital breast tomosynthesis, with a voxel size of $(50\ \mu m)^{3,35}$.

The feasibility of decreasing radiation exposure in PCD imaging technology has also been demonstrated in lung tissue and shown higher contrast, lower noise levels, and ultimately better diagnostic quality than energy-integrating detector CT imaging[38]. Therefore, PCD CT imaging is expected to be particularly interesting in future low-dose lung cancer screening studies. A recent study has reported the development of a prototype PCD CT scanner with a relevant dental filling artifact reduction[39]; this method, if validated in clinical studies, would have enormous potential in head and neck cancer staging, wherein artifacts are the primary reason for cancer misclassification and recurrence of missed tumors[40].

Phase-contrast-based synchrotron CT imaging

Another emerging technology in preclinical medical research is phase-contrast-based synchrotron CT imaging, performed at synchrotron radiation beamlines[41,42]. This method is sensitive to light elements (hydrogen, carbon, nitrogen, and oxygen) whose X-ray phase shift cross section is much larger than the X-ray absorption cross section; therefore, phase maps from an X-ray interferometer may be used to detect specific interference patterns and subsequently reveal microscopic soft tissue details at nanometer scale without a need for specific tissue staining[41]. Although such analyses have been restricted to only very small sections of biological specimens, the first high-energy (6-GeV), fourth-generation synchrotron source at the European Synchrotron Radiation Facility has allowed

for the scanning of human organs in toto[42,43] (**Figure 2**). This non-destructive technique may provide unprecedented detail of the extent of oncological disease, thus aiding in studies of tumor infiltration patterns and changes in the tissue microenvironment around tumor cells in whole human organs and whole rodents.

Outlook

The exciting new possibilities of PCD CT imaging with increased resolution and decreased radiation exposure, as well as additional contrasts, are beginning to be explored in the first large-scale clinical studies, which are expected to shape the future of CT imaging[44,45]. Although only few PCD CTs are currently available, many more are expected to be found in hospitals and radiology cabinets. Their potential and pitfalls are expected to determine future oncological disease diagnosis, staging, and monitoring. Simultaneously, progress in *ex vivo* phase-contrast-based synchrotron CT imaging with imaging of whole human organs is expected to facilitate exploration of cancer growth patterns in greater detail, thereby providing a microstructural basis to detect, interpret, and quantify CT imaging patterns in oncology.

MRI

MRI has markedly advanced since the first recorded nuclear magnetic resonance (NMR) signal in an anesthetized rat was reported by Jackson and Langham in 1968[46]. Raymond Damadian proposed and patented an "Apparatus and method for detecting cancer in tissue" relying on NMR technology in 1974, on the basis of his findings that the spin-lattice (T1) and spin-spin (T2) magnetic relaxation times differed between normal rat tissue and sarcoma and hepatoma tissue[47]. Likewise, other groups found differing NMR relaxation times between healthy and neoplastic tissue[48]. Several years after Paul Lauterbur produced the first MR images in 1973[49], the first clinical MRI was introduced, thus eventually leading to the high-field machines with 1.5 Tesla and 3 Tesla magnetic field strengths in clinical use today. Simultaneously, apart from the fundamental T1- and T2-weighted sequences, many new MR sequences have been developed to elucidate various tissue properties. To comprehend their roles in translational cancer research, we distinguish between weighted and quantitative imaging MRI sequences (**Figure 3**).

In weighted sequences, the contrast can be optimized by varying specific sequence-inherent parameters, e.g., the echo time (TE) for T2-weighted sequences in the range of T2[50]. The typical weighted sequences are T1-, T2-, and proton density (PD) weighted sequences, with short repetition time (TR) and short TE, long TR and long TE, and long TR and short TE, respectively. Other weighted sequences are diffusion-weighted imaging (DWI) and T2*-weighted and/or susceptibility-weighted imaging (SWI) sequences, which were developed in the late 1980s and 1990s and are now part of the standard MRI protocols in cancer imaging. Steady-state free precession MRI sequences maintain a residual transverse magnetization between successive MRI pulse cycles to generate a mixed contrast between T2 and T2* weighting, and are used primarily in dynamically changing organs such as the heart[51].

Quantitative sequences enable acquisition of tissue-specific physical entities or parameters that therefore are prone to changes with alterations in tissue composition, e.g., owing to metabolic changes or tumor cell infiltration. These sequences have a functional quality that cannot be attributed to conventionally structural sequences, with the sole exception of the apparent diffusion coefficient (ADC), a quantitative parameter obtained in DWI sequences. Apart from ADC mapping and dynamic-contrast enhanced (DCE) or dynamic susceptibility contrast (DSC) MR perfusion sequences, all these functional, quantitative sequences are not yet part of standard oncological MRI protocols. Their roles in translational cancer imaging are reviewed below.

In addition, model-based quantitative imaging methods provide indirect information on the voxel-inherent microstructure. They are motivated by small magnetic field inhomogeneities that produce local changes in magnetic susceptibility and diffusion, both of which influence the MR signal decay. Measurements of detailed MR signal decay curves therefore allow for quantification of the underlying microstructure, e.g., microvascular density or axonal myelination.

DWI, diffusion-tensor imaging, and intravoxel-incoherent motion imaging

DWI is currently integral part of most MRI protocols in oncologic imaging for a variety of tumors, e.g., brain tumors, prostate cancer, or metastatic disease in general[52]. Increased tumor cellularity restricts the diffusion of water molecules around tumor cells, thus resulting in a hyperintense signal in
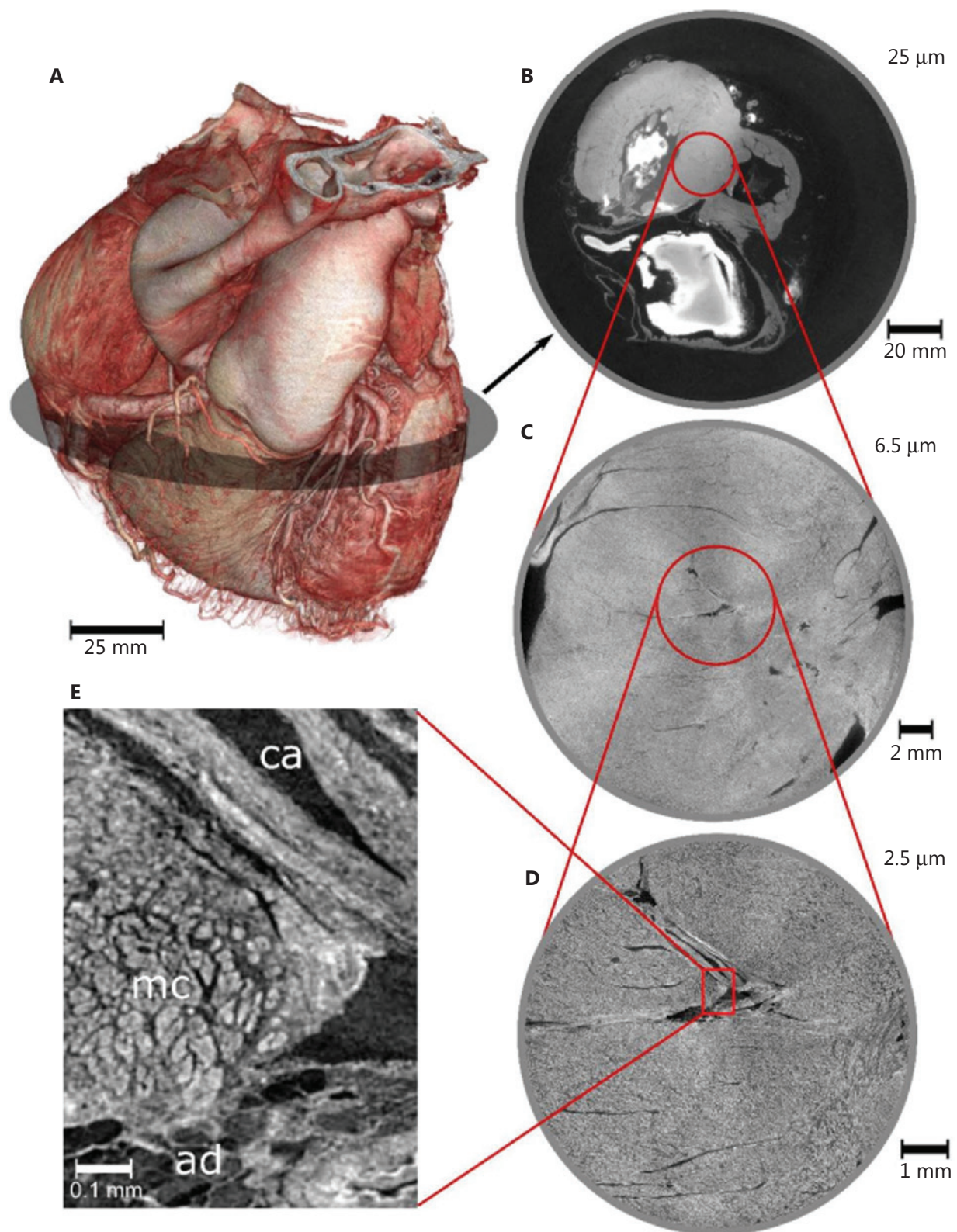
Figure 2 Phase-contrast-based synchrotron CT images of an intact human heart. (A) Intact human heart, and magnified cross-sections with voxel sizes of (B) 25 μm, (C) 6.5 μm, and (D) 2.5 μm, and (E) magnification of the image in (D), revealing the local arrangement of ventricular myocytes (mc), a coronary artery (ca), and adipose tissue (ad). Adapted from Ref.[233] (CC BY-NC 4.0 license).

Magnetic resonance imaging

Weighted imaging									
	T1w	T2w		T2*w	SSFP	PD	DWI	SWI	

Quantitative imaging										
	T1r	T2r	T2*r	QSM	DTI	DCE/DSC	MRE	ASL	MRS	CEST

Model-based quantitative imaging			
	VSI/VAI	Microvascular radius mapping	NP density mapping	Axonal myelination

Figure 3 MRI sequences used in translational cancer research, including weighted sequences, quantitative sequences, and model-based quantitative microstructural imaging sequences. T1w, T1-weighted imaging; T2w, T2-weighted imaging; T2*w, T2*-weighted imaging; SSFP, steady state free precession imaging; PD, proton spin density imaging; DWI, diffusion-weighted imaging; SWI, susceptibility-weighted imaging; T1r, T1 relaxation mapping; T2r, T2 relaxation mapping; T2*r, T2* relaxation mapping; QSM, quantitative susceptibility mapping; DTI, diffusion tensor imaging; DCE, dynamic contrast-enhanced MR perfusion imaging; DSC, dynamic susceptibility contrast MR perfusion imaging; MRE, magnetic resonance elastography; ASL, arterial spin labeling imaging; MRS, magnetic resonance spectroscopy; CEST, chemical exchange saturation transfer imaging; VSI, vessel size imaging; VAI, vascular architecture imaging; NP, nanoparticles. Further details are in the main text.

DWI images with higher b-values. This sensitivity to diffusion results from the applied b-values whose quality depends on the gradient properties during the pulse sequence design. The role of DWI in differentiating malignant neoplastic tissue from healthy tissue or predicting treatment response has been investigated in most, if not all, tumor types[52-57]. Although its resolution (2–5 mm^2 in plane) is typically lower than those of structural sequences, its b-value dependent contrast with cell-rich tumor tissue and its ability to provide tissue-specific ADCs have demonstrated great success in identifying tumor tissue. An increasing number of MRI tumor protocols now incorporate DWI in their tumor grading systems, most prominently the Prostate Imaging Reporting and Data System (PI-RADS) classification for prostate cancer[58], the Breast Imaging Reporting and Data System (MRI BI-RADS) classification for breast cancer[59], the Myeloma Response Assessment and Diagnosis system (MY-RADS) classification for myeloma[60], and the Ovarian-Adnexal Reporting Data System (O-RADS) MRI score for ovarian cancer[61].

Owing to its relatively fast acquisition time and superior contrast, DWI is also being investigated for its use in MRI cancer screening protocols, specifically in whole-body MRI cancer screening in cancer predisposition syndromes[62]. However, the roles of DWI and of MRI in general in screening common cancer types such as breast, prostate, and lung cancer remains controversial[63-65].

Diffusion tensor imaging, in contrast to DWI, considers diffusion along multiple directions in three-dimensional space. Because water diffusion in biological tissue is often anisotropic, and not isotropic, i.e., equal in all directions, the concept of a diffusion tensor captures and quantifies this (fractional) anisotropy, thus enabling investigation of preferred tracts of diffusion, e.g., along neuronal fibers in brain tissue or peripheral nerves[66,67]. Although used primarily in neuro-oncology[68], this method has also been shown to be beneficial in determining the histological grade of oral carcinoma[69]; discriminating between small-cell lung cancer and non-small cell lung cancer brain metastases[70]; correlating with Gleason scores in prostate cancer[71]; or predicting parametrial infiltration in cervical cancer[72].

Diffusion within an MR voxel that differs from (extracellular) water diffusion, such as blood circulation within the capillaries, is termed intravoxel incoherent motion (IVIM). IVIM leads to attenuation of the diffusion MR signal at low b-values, because the diffusion coefficient, or pseudodiffusion, associated with blood flow is larger than the diffusion coefficient of water, thus effectively leading to a slightly larger ADC value[73]. Pseudodiffusion and diffusion can be separated, thereby enabling determination of a flowing blood volume fraction (fIVIM: fractional IVIM) to obtain estimates of blood perfusion without the use of external contrast agents (see Section 2.2.4)[74]. Owing to the abnormal microvasculature in tumors, IVIM is increasingly being applied in oncological settings[75] mostly in rectal, pelvic, and hepatic cancers, and fIVIM has been found to strongly correlate with microvessel density[75,76]. Its role in common cancer types, such as breast and prostate cancer, is currently being evaluated[77,78].

Susceptibility-weighted imaging and quantitative susceptibility mapping

SWI is based on the differences in local magnetic susceptibilities in biological tissue, which lead to phase shifts at

sufficiently large echo times[79,80]. However, across different MR vendors, SWI typically denotes a high-resolution susceptibility-enhanced sequence that is not necessarily processed with phase information, thus resembling a T2*-weighted sequence. This method is used in standard imaging protocols in neuroradiology to detect microbleeds or thrombi. However, it has rarely been used outside of neuroradiological imaging applications. Intratumoral susceptibility signals in brain tumors have been attributed to microbleeds and abnormal vasculature, and may aid in differentiating high- and low-grade gliomas[81,82]. This method has been shown to provide limited diagnostic benefit over T1-weighted sequences in the evaluation of melanoma brain metastases[83], in which SWI artifacts inside metastases are attributed primarily to microbleeds. Recently, SWI has been used to differentiate osteolytic from osteoblastic spine metastases[84]; to show intratumoral hemorrhages in uterine sarcomas as a diagnostic differentiator[85]; or to evaluate treatment response in patients with prostate cancer receiving androgen deprivation therapy[86].

Quantitative susceptibility mapping, the quantitative extension of SWI, has been proposed to provide local magnetic susceptibility values and evaluate their spatial distribution[87,88]. This method has been investigated as a potential biomarker of tumor severity in glioma, in which basal ganglia iron content increases with glioma severity[89]. Further studies are needed to assess its utility in oncological research and clinical imaging.

T1-, T2-, and T2* mapping sequences

Relaxation time mapping sequences sample the MR signal decay to obtain measures for the relaxation times[90-92]. Although T1, T2, and T2* mapping techniques were initially used primarily in cardiac imaging to adequately characterize myocardial edema and disease[91], or cardiac iron overload[92], they have also been applied in oncology[93]. Their use beyond cardiac imaging has increased, owing to better reconstruction and k-space sampling techniques, e.g., for mapping peritumoral infiltration zones in glioblastoma and anaplastic astrocytoma with T2 mapping[94], or to identify histological types of lung cancer with T1 mapping[95]. T1 mapping has also been used to predict Gleason scores in prostate cancer[96], whereas T2 mapping in prostate cancer has been used to differentiate between healthy and cancerous gland tissue[97].

The quantitative property of relaxation time maps, *via* a combination of several relaxation times, or ideally with other quantitative parameters such as ADC values, makes them well-suited to characterize heterogeneous tumor tissue and also to future robust extraction of tumor-intrinsic imaging patterns, e.g., in radiomics and deep-learning analyses of pathological tissue, as described below. A multiparametric quantification may uncover differences between specific disease subgroups within multidimensional parameter spaces that would otherwise not be detected, and therefore aid in further integrative diagnostic endeavors. The potential role of multiparametric MR mapping in breast, prostate, and liver cancer has been reviewed[98-100]. Quantitative parameters (T1, T2) from synthetic breast MRI have been found to discriminate among breast cancer receptor statuses or proliferation rates[101], whereas combined T1/T2 relaxation time mapping, ADC mapping, tumor size, and cancer subtype modeling have been shown to effectively predict pathological response in breast cancer after one neoadjuvant chemotherapy cycle[102]. In prostate cancer, T2 mapping has revealed significantly lower T2 values in cancerous regions[103], and has shown high diagnostic accuracy in differentiating between chronic prostatitis and cancer[104]. In contrast, T1 mapping has been found to predict Gleason scores[96]. In liver cancer, multiparametric MRI (T1, T2 relaxation times) has been found to be useful in detecting sinusoidal obstruction syndrome after oxaliplatin-based chemotherapy[105]. T2 relaxation times have been shown to be more sensitive and accurate in identifying malignant liver lesions than ADC values[106], whereas T1 mapping has enabled differentiation among tumorous liver regions according to extracellular matrix composition in a rabbit hepatic cancer model[107], as well as accurate detection of liver metastases in a mouse model at 7 Tesla[108].

MR perfusion and permeability sequences

Many tumors thrive with microvascular proliferation, most prominently the aggressive brain tumor glioblastoma, which requires MR techniques to image and quantify intra- and peritumoral perfusion or the permeability of leaky tumor vessels. DSC imaging typically uses single-shot (or multi-shot) echo-planar imaging with repetition times of 1–2 seconds over a contrast agent bolus. The local tissue contrast agent concentration can then be inferred from the altered MR signal (during contrast agent bolus passage) in relation to its baseline signal[109], thus allowing for the calculation of perfusion parameters such as mean transit time, local blood volume and flow, and time-to-peak. DSC imaging is currently used almost exclusively in brain imaging to reveal cerebral hemodynamics

and show increased blood volume in cerebral tumor tissue[110]. This method is part of the standard MRI protocol in glioma and other malignant brain tumors[111]. However, it has also been used to differentiate benign from malignant soft tissue tumors[112], or benign from malignant head and neck tumors or parotid tumors[113,114]. Its potential to describe tumor vasculature in other tumor entities still must be explored.

DCE MRI uses baseline T1 mapping and subsequent acquisition of T1-weighted images during contrast agent bolus passage. The MR signal change can then be associated with the local contrast agent concentration *via* pharmacokinetic models such as the extended Tofts model[115,116], which assume an exchange in contrast agent particles between the blood vessel plasma and the extravascular space, by using the plasma-extravascular space transfer constant K-trans as a measure for permeability. DCE MRI is particularly established in imaging of breast and prostate cancer, for which DCE is part of the standard MRI protocols, and its interpretation is included in the BI-RADS and PI-RADS criteria. This method is also frequently used in imaging intracranial tumor imaging[117], liver imaging[118], and head and neck cancer imaging[119].

Blood-oxygen-level-dependent MRI

The differing magnetic properties of oxygenized and deoxygenized hemoglobin were first described by Pauling and Coryell in 1936[120]: oxyhemoglobin is diamagnetic, whereas deoxyhemoglobin is paramagnetic, thus signifying their different magnetic susceptibilities. This effect was first used by Ogawa to develop a blood-oxygen-level-dependent (BOLD) imaging contrast between arterial (oxygenated) and venous (deoxygenated) blood[121]. Because firing neurons require blood-delivered oxygen to generate energy, in the so-called hemodynamic response, BOLD contrast can be used to detect task-activated brain regions in functional MRI (fMRI), which is extensively, although controversially, used in psychiatric and psychological studies[122,123]. However, typically on the basis of multi-gradient-echo sequences, BOLD imaging is easily implementable in clinical routines, and it can be used to measure tumor hypoxia, a hallmark of cancer associated with therapy resistance and tumor progression[124]. Hypoxia also affects the T1 relaxation time in tumors, thus giving rise to tissue-oxygen-level-dependent (TOLD) MRI contrasts, wherein an inhaled gas challenge between air and 100% oxygen leads to heterogeneous changes in T1 relaxation rates within the tumor tissue[125]. For instance, a strong association

the between BOLD response and partial pressure of oxygen in prostate cancer, and between TOLD and delayed tumor growth after irradiation therapy[126], have been demonstrated. More recent developments include the combination of TOLD and DCE MRI to identify tumor regions refractory to oxygen challenge within renal cancer xenografts, to more accurately determine tumor hypoxia[127]; the differentiation between musculoskeletal tumors through power spectrum analyses of the BOLD time series signals[128]; and the induction of cerebrovascular dysregulation, according to glioma grade, through time-shifted fMRI traces[129].

Magnetic resonance elastography (MRE)

MRE is a phase-contrast-based MRI method that quantifies the mechanical properties of biological tissue, such as elasticity or stiffness. Because the stiffness changes in most tumors can be quantified by the calculation of a shear and elastic modulus, MRE is increasingly being used in experimental oncological imaging, e.g., in brain tumors[130]. It relies on the generation of mechanical waves, which are generated with dedicated vibrating devices placed on patients' bodies[131]. MRE functions with many pulse sequences, including spin echo and gradient-recalled echo sequences, with or without echo-planar imaging, and is typically performed at frequencies between 20 and 100 Hz in clinical imaging, and 200 and 1,500 Hz in preclinical imaging, preferably with 3.0 Tesla scanners to achieve higher signal-to-noise and contrast-to-noise ratios[131]. The resolution of MRE is usually lower than that of conventional MR images, and it assumes an isotropic material composition, which is clearly not the case for many tissue types such as white matter fibers or muscle tissue. Like ultrasound elastography, MRE is used in breast imaging to detect early changes in tissue stiffness due to neoplastic disease[132]. However, most applications to date have been in brain and liver imaging[130,133]. Recent studies have indicated that MRE can be used to assess therapy outcomes and tissue damage before and after microwave ablation of liver tumors[134], and liver stiffness has been found to be a predictor of early recurrence in hepatocellular carcinoma after therapy[135]. Simulation and phantom studies of MRE imaging have linked MRE parameters to intratumoral pressure[136], and experimental preclinical studies have indicated that MRE may be suitable for specifically studying tumors with nondestructive growth patterns, such as prostate cancer[137].

Arterial spin labeling (ASL)

ASL technique does not require external contrast agent but instead uses labeling of blood water spins in larger arteries with specific radiofrequency pulses to obtain perfusion measures, such as blood flow and blood volume in downstream tissue areas, through the subtraction of labeled and control images[138]. Several ASL techniques have been proposed. The most common variant is pseudocontinuous ASL, which uses multiple short pulses during continuous labeling of water molecules that pass through a labeling plane. Most applications of ASL are in translational or preclinical research; however, some institutes use ASL measurements to assess perfusion in pediatric tumors without a need for contrast agent administration[139]. Owing to difficulties in finding adequate labeling planes, ASL is typically used in brain, head and neck, and renal tumors[140-143], but has also been investigated in other organs, such as the liver[144], heart[145], and prostate[146]. The low resolution of ASL images with respect to that of conventional MR sequences limits its use in oncological screening; however, the benefit of avoiding contrast agent administration is expected to result in increased use of this technique in pediatric imaging, in oncological patients with many follow-up exams, and in oncological wards aiming to replace contrast-agent-based perfusion MRI with less expensive imaging. Novel pulse sequence designs and deep learning techniques to improve ASL robustness and accuracy are currently being developed[147].

Magnetic resonance spectroscopy (MRS) and chemical exchange saturation transfer imaging

MRS measurements enable probing of metabolic tissue properties *in vivo*. MRS is frequently used in clinical settings, e.g., to determine metabolite content in brain tumors[148]. This method is based on a chemical shift of the local resonance frequency in the external, static magnetic field, because of the shielding effect of electron clouds that are associated with bonding electrons of the prevalent molecules within the tissue. The effect is proportional to the magnetic field strength and therefore is particularly relevant at high and ultra-high field strengths, such as 3 Tesla and 7 Tesla. The resulting spectrum of molecule peaks reveals the molecular composition of the probed tissue. For instance, in aggressive brain tumor glioblastoma, increases are observed in the peaks of choline, a marker of cellular membrane turnover; lactate, a marker of anaerobic metabolism; and lipids, a markers

of severe tissue damage and necrosis, whereas N-acetylaspartate (NAA), a marker of neuronal viability, is decreased[149]. The use of MRS is often limited to low-grade gliomas in neuroimaging, to refine lesion differential diagnostics, as well as to single large tissue voxels to produce robust and reproducible spectra; otherwise, MRS is used primarily in research studies. However, with advanced MRS processing techniques, whole-brain MRS is clinically feasible and may be used to study large-scale metabolic alterations during tumor growth[12].

Furthermore, MRS has been applied in many other tumors, particularly prostate cancer, thus revealing low levels of citrate, a key metabolite in oxidative phosphorylation[150], in colorectal cancer[151], cancers of the head and neck[152], or breast cancer with elevated choline peaks[153].

The recent development of chemical saturation exchange (CEST) imaging in brain tumors, e.g., to identify genetic markers such as isocitrate dehydrogenase mutation status or 1p/19q deletion status in gliomas, has received substantial attention in the oncological imaging community[154]. CEST imaging enables mapping of tissue pH levels *via* amide proton transfer CEST[155], wherein backbone amide protons of mobile proteins and peptides provide the endogenous CEST contrast[156]. Further applications include glucose CEST (glucoCEST)[157], to detect intercellular glucose delivery and transport; the first applications outside brain tissue, e.g., detection of ductal pancreatic adenocarcinoma[158]; kidney assessment *via* renal pH levels[159]; prostate cancer detection[160]; and diagnosis of breast cancer *via* glucosamine CEST in clinical settings[161].

Advances in cardiac MRI

Cardiac imaging in oncology is used not only to characterize cardiac malignant masses, but also cardiac dysfunction or cardiotoxic effects associated with cancer therapy, including peripheral vascular disease and vascular dysfunction[162,163]. Recent advances in cardiac MRI have seen the development of simultaneous multi-parametric acquisition and reconstruction techniques (SMART) to accelerate acquisition times in cardiac imaging. SMART is particularly helpful in patients with complicated heart rhythms or with poor compliance during breath-hold instructions[164]. Simultaneous collective acquisition of several MR parameters such as T1 and T1 relaxation time would therefore significantly improve cardiac MRI efficiency[165]. Further new and emerging imaging techniques include electrocardiogram gated double inversion recovery fast spin echo sequences (or "black-blood" sequences), which can more reliably be used

1574

Kurz and Schlemmer. Imaging in translational cancer research

for characterization of cardiac masses or detection of cardiac edema due to nulling of blood[166]; detection of coronary artery disease, as a cardiotoxic effect of cancer-associated therapy with high speed coronary magnetic resonance angiography or ultrafast imaging of the coronary arteries[167,168]; visualization of pulmonary arteries and their implication in oncological disease through 3D pulmonary MR angiography[169]; and evaluation cardiac flow velocities at high spatial and temporal resolution with four-dimensional flow MRI[170]. These techniques are currently being established to, e.g., evaluate the role of anthracycline-induced cardiotoxicity[171], or detect early cardiotoxicity during immuno- and radiotherapy[172].

Model-based quantitative imaging

NMR signal decay is influenced by local magnetic susceptibility gradients and water diffusion, both of which depend on the microstructural arrangement of tissue, as first described 3 decades ago for local susceptibility differences between blood-filled idealized, i.e., cylindrical, vascular structures and static water molecules (static dephasing)[173]. This method is still widely used in MR signal decay simulations. However, MR signal modeling can now be used for increasingly complex arrangements of vessels and/or small particles such as iron-oxide nanoparticles[174,175], and with the inclusion of diffusion effects[176-181], in microstructural quantification *in vivo*[182,183], also termed histological MRI (hMRI)[184,185]. Correlative analyses of MR signal decay and microvascular arrangements in tumor tissue can be studied with these modeling approaches and dedicated microscopy experiments (**Figure 4**)[185-187]. Similarly, myelinated axons and fiber tracts can be quantified by using the effects of anisotropic susceptibility within and around the myelin sheath[188,189], and advanced models of microstructure derived from diffusion-weighted imaging, using multi-compartment environments as in nerve fibers, have been described[190-193].

However, the increasingly complex theoretical models are often too computationally intensive to be implemented in routine clinical imaging. Moreover, multiparameter models may produce relevant fitting errors that do not allow for robust and reliable microstructure quantification. This gap is being filled by empirical signal models that obtain information on microvascular arrangements *via* surrogate parameters, such as vessel size and vessel architectural imaging (VSI, VAI)[194-196]. These methods are being used to detect microvascular changes, e.g., during antiangiogenic treatment in glioblastoma[197].

Hybrid imaging: positron-emission tomography CT and MRI

PET is a functional imaging method that uses radioactive tracers to visualize biological processes within the human body. The radiotracers frequently used for routine PET imaging in oncology are ^{18}F-fluorodeoxyglucose (FDG) and prostate-specific membrane antigen (PSMA); their roles in cancer phenotyping and recommendations for their use in oncological imaging have been reviewed[198,199]. Increased local FDG uptake in the PET images reflects increased regional glucose transporter activity on a cellular level, which in turn indicates increased cellular metabolic activity (**Figure 5**)[200], as observed as an unspecific finding in a variety of metabolic active and growing cancers and their metastases. Consequently, FDG-PET imaging is a valuable tool to provide diagnostic certainty when CT or MRI morphologic findings are otherwise unclear and lack functional information on biologic activity. In contrast, CT and MRI add essential anatomic information that PET is lacking. Hybrid imaging approaches are therefore synergistic: PET has been combined with CT (PET-CT) or MR (PET-MR) to enable fusion of CT and MRI images with areas of increased metabolic activity. PET-CT is the modality of choice for the staging and therapy monitoring of many cancers, such as head and neck, breast, lung, esophageal, colon cancers, melanomas, and aggressive lymphomas[201-203]. PET-CT imaging is currently being investigated for its clinical benefits in a wide range of malignant tumors, e.g., melanoma staging[204], bone and soft tissue tumors[205,206], and distant metastases and recurrence of head and neck tumors[206].

PET in combination with MRI is available only at few hospitals and research centers. However, the prospects of correlating metabolic functional imaging with functional and structural MRI parameters may be attractive not only for answering research questions but ultimately for translation to clinical imaging[207]. E.g., FDG-PET-MRI has been found to outperform MRI in evaluating tumor size and nodal metastases in rectal cancer[208], and MRI and CT for nodal staging in breast cancer[209].

Apart from FDG and PSMA, several other tracers are currently being used and investigated in PET imaging, most prominently FAPI, which uses the tumor expression of fibroblast-activating protein (FAP) to diagnose and stage patients with cancers of the stomach or pancreas, and cholangiocarcinoma[210]. Other tracers are ^{18}F-fluoroethyl-L-tyrosine (FET) and ^{11}C-methionine (MET), which correlates with microvessel density in proliferating
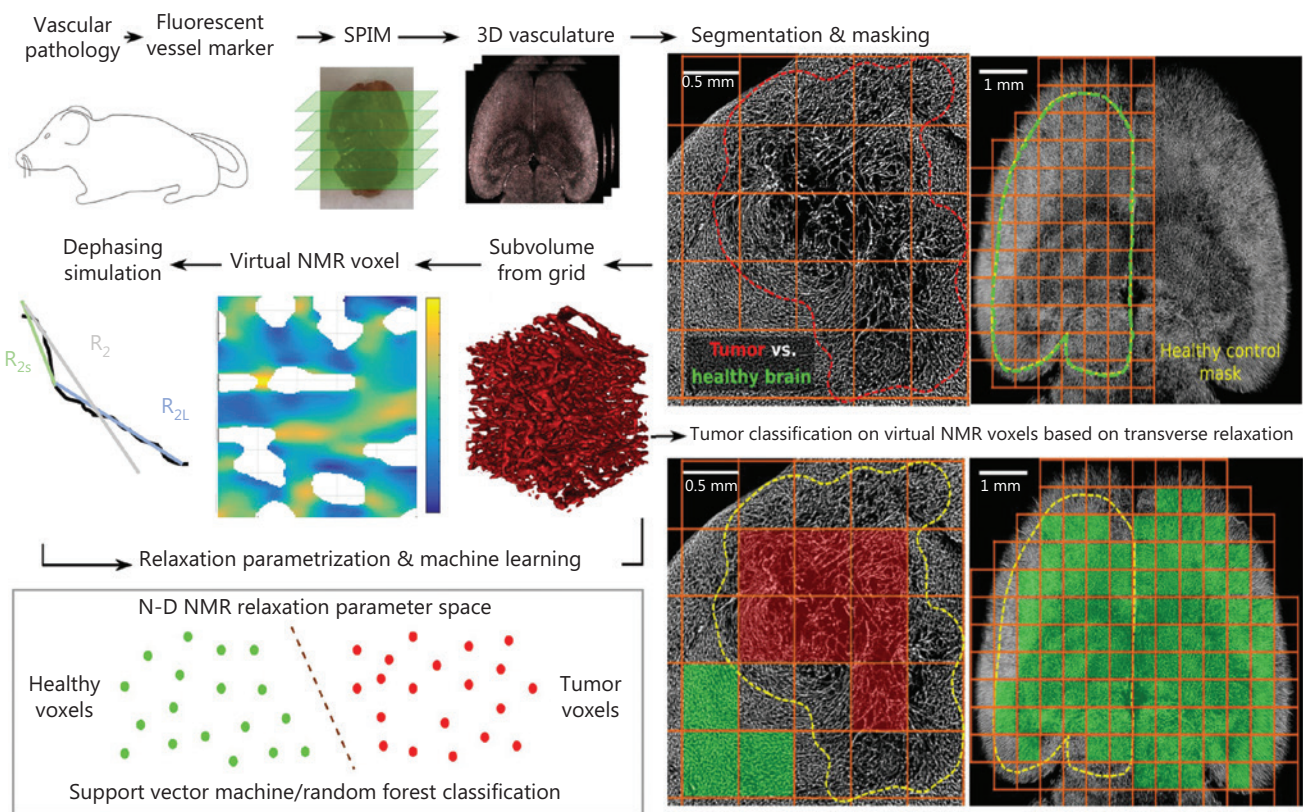
Figure 4 Virtual NMR voxel tumor classification. Left panel, top row: mice are injected with a fluorescent vessel marker, and subsequent brain resection, brain clearing, and selective plane illumination microscopy (SPIM) are used to visualize three-dimensional microvasculature; details have been described.[186] Abnormal microvasculature in the tumor area (here, U87 glioblastoma) is delineated and partitioned into voxels with a 0.5 mm side length, which correspond to a voxel in a high-resolution MRI image stack. Similarly, a control mask is created on a healthy hemisphere and partitioned as well (far right, top row). Left panel, middle row: the microvasculature in each voxel is segmented, and spin dephasing is performed on the specific vascular arrangements to reveal multi-exponential MR signal decays (indicated with a MR signal decay relaxation rate component for short times, R_{2s}, and for long times, R_{2L}). Subsequently, relaxation parametrization occurs for each voxel, and can be used to train the classification of voxel vascular geometries into healthy and cancerous geometries (lower row) by using support vector machines or random forest classifiers; see also Ref.[185] Adapted from Ref.[186] (CC BY 4.0 license).

cells, both of which are used in glioma imaging; ^{68}Ga-DOTATOC (DOTA^0-Phe^1-Tyr^3-octreotide), a somatostatin analog used to detect neuroendocrine tumors[211]; and ^{11}C-metomidate PET, which is used to detect adrenal masses[212].

Medical image computing in translational cancer research

Recent years have seen an astonishing increase in supervised and unsupervised computational medical image analyses to detect, segment, and classify tissue pathologies in oncology[213]. Together with other high-throughput analyses such as genomics, proteomics, or metabolomics, artificial intelligence based methods such as radiomics and deep-learning techniques have emerged as powerful tools in oncology. These methods enable extraction and quantification of imaging characteristics in radiological imaging, specifically pattern or texture analysis, which computationally allocates imaging signatures to pathological imaging changes[214,215]. Combined radiomics features (RF) can be used to predict disease status and changes during specific therapy regimens, on the basis of machine learning approaches in high-throughput agnostic analyses (**Figure 6**)[216]. Because RF based imaging is increasingly commonly used and, access to computational equipment and powerful computational hardware is increasing, RF based image interpretation is expected to be applied in clinical diagnostics in the coming years[217].
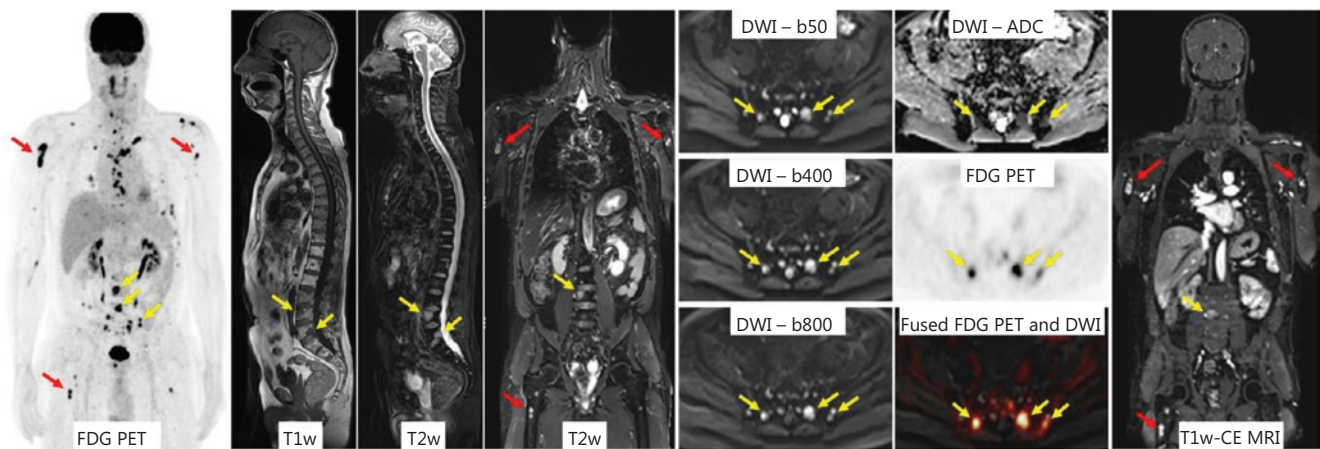
Figure 5 PET-MRI in a patient with multiple myeloma. Focal bone lesions are visible in the axial skeleton (yellow arrows) and in the proximal upper and lower extremities (red arrows) in ^{18}F-fluorodeoxyglucose (FDG) PET, in DWI images at different b-values (b = 50, b = 400, b = 800), in the ADC map, and in fat saturated contrast-enhanced T1w images (T1w-CE MRI). The combined structural, metabolic, and MR functional (DWI) information enables multiparametric, multifunctional characterization of the multifocal disease activity. Adapted from Ref.[200] (CC BY 4.0 license).
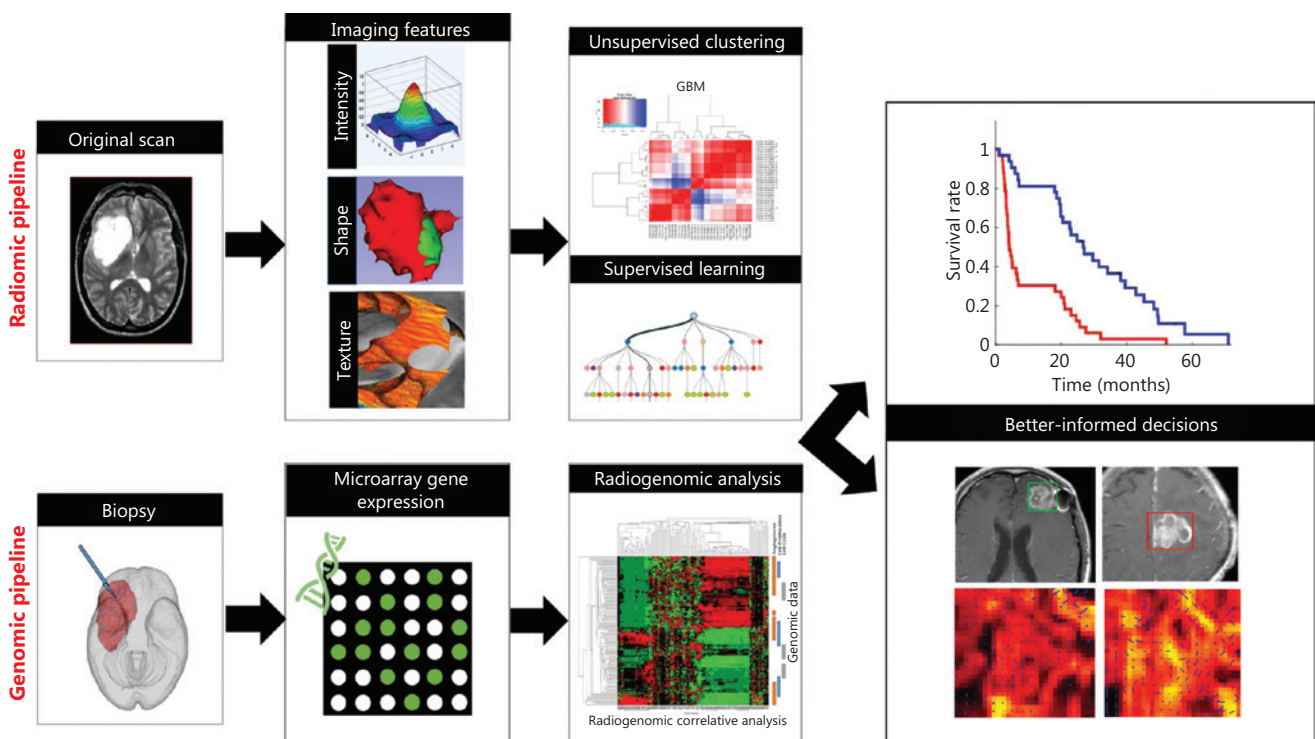

Figure 6 Standard radiomics pipeline for brain tumors. Top row: the original scan is normalized, and imaging features are extracted on the basis of IBSI criteria[230]. Subsequently, both unsupervised or supervised learning can be performed to classify radiomic features (RF) into those that correlate with therapy responders or non-responders, or with overall survival. Bottom row: gene expression profiles from tumor biopsies can likewise be screened for correlations with RFs to eventually identify RFs that may predict therapy success, recurrence, or overall survival, and therefore may affect clinical decision-making. Adapted from Ref.[222] (CC BY 4.0 license).

Initially, RF extraction was performed in neuroimaging, e.g., to achieve radiomic profiling of glioblastoma tissue to identify imaging predictors of patient survival and anti-angiogenic treatment response[218,219]. Many other studies have applied RF extraction to all types of tumors and imaging modalities, most prominently lung tumors[220], often in combination with genomic profiling, termed radiogenomics[221]. In many cases, relevant RFs have been found to discriminate between different tumor classes, e.g., low- and high-grade gliomas[222]; to be highly sensitive to cancerous tissue as in breast cancer[223]; or to predict treatment response in prostate cancer[224]. Several prospective clinical trials are currently underway to test the reliability and reproducibility of RFs in different centers and for machines of different vendors[225]. However, radiomics has not yet been applied in clinical imaging.

Developments in machine learning algorithms *via* artificial neuronal networks with many layers, or deep learning, often with so-called convolutional deep neural networks, have generated networks that can be trained to independently detect, segment, or classify image-based pathologies[226,227]. The recent explosion of deep learning studies in oncology has been due to increasing access to large databases of image material, such as the Cancer Imaging Archive of the NIH National Cancer Institute; to technological developments in graphics processing units; and to a vibrant and dynamic community spanning diverse disciplines such as mathematics, computational engineering, radiology, biology, or physics.

Although the applications of machine learning in medical image computing are manifold and promising, one major disadvantage is the lack of reproducible results, which may be attributed to the non-standardized RF parameters in radiomics, or to a non-negligible inter-scan variability with different acquisition parameters (e.g., in MRI, different flip angles, matrix size, TR/TE variations, field strength, etc.); non-expert annotation of imaging data and therefore annotation bias; and different and/or non-standardized machine learning models, many of which are prone to overfitting[228,229].

For radiomics, the research community therefore has sought to establish standardized parameters in RF selection *via* the image biomarker standardization initiative (IBSI)[230], and to build large databases to provide access to sufficiently large medical (anonymized) patient databases to allow broad testing of new algorithms. One commonly cited example is the Cancer Genome Atlas Glioblastoma multiforme data collection[231].

Yet, with increasingly complex, often deep-learning-based, predictive modeling approaches, radiomics and deep learning feature selection is a purely statistical concept that focuses on predictive power rather than the biological meaning of these imaging characteristics, thus increasing the disconnect between radiological diagnostic decision-making in routine clinical practice and RF-informed image interpretation. This gap is expected to affect, and eventually limit extensive translation into routine clinical imaging[232].

Conclusion

The ongoing advances in cross-sectional imaging have significant impact on the progress in translational cancer research. New developments such as CT photon-counting detectors, multiparametric microstructural MRI, multimodal and hybrid imaging approaches, as well as their combination with machine-learning-based image analysis methods provide increasingly detailed insight into tumor biology and heterogeneity. Integrative assessment with the aid of bioinformatics enables combining structural imaging signatures with functional imaging characteristics, genomic or metabolomic profiles, and various patient clinical data. These advances in oncologic imaging are key pillars for future precision oncology.

Conflict of interest statement

No potential conflicts of interest are disclosed.

References

1. Fass L. Imaging and cancer: a review. Mol Oncol. 2008; 2: 115-52.
2. O'Connor JPB, Aboagye EO, Adams JE, Aerts HJ, Barrington SF, Beer AJ, et al. Imaging biomarker roadmap for cancer studies. Nat Rev Clin Oncol. 2017; 14: 169-86.
3. Hsieh J, Flohr T. Computed tomography recent history and future perspectives. J Med Imaging (Bellingham). 2021; 8: 052109.
4. White NS, McDonald C, Farid N, Kuperman J, Karow D, Schenker-Ahmed NM, et al. Diffusion-weighted imaging in cancer: physical foundations and applications of restriction spectrum imaging. Cancer Res. 2014; 74: 4638-52.
5. Farolfi A, Calderoni L, Mattana F, Mei R, Telo S, Fanti S, et al. Current and emerging clinical applications of PSMA PET diagnostic imaging for prostate cancer. J Nucl Med. 2021; 62: 596-604.
6. Villa A, Klein B, Janssen B, Pedragosa J, Pepe G, Zinnhardt B, et al. Identification of new molecular targets for PET imaging of the microglial anti-inflammatory activation state. Theranostics. 2018; 8: 5400-18.
7. Riola-Parada C, García-Cañamaque L, Pérez-Dueñas V, Garcerant-Tafur M, Carreras-Delgado JL. Simultaneous PET/MRI vs PET/CT

in oncology. A systematic review. Rev Esp Med Nucl Imagen Mol. 2016; 35: 306-12.

8. Ming Y, Wu N, Qian T, Li X, Wan DQ, Li C, et al. Progress and future trends in PET/CT and PET/MRI molecular imaging approaches for breast cancer. Front Oncol. 2020; 10: 1301.

9. Papadimitroulas P, Brocki L, Christopher Chung N, Marchadour W, Vermet F, Gaubert L, et al. Artificial intelligence: deep learning in oncological radiomics and challenges of interpretability and data harmonization. Phys Med. 2021; 83: 108-21.

10. Musa IH, Afolabi LO, Zamit I, Musa TH, Musa HH, Tassang A, et al. Artificial intelligence and machine learning in cancer research: a systematic and thematic analysis of the top 100 cited articles indexed in Scopus database. Cancer Control. 2022; 29: 10732748221095946.

11. Weinberg BD, Kuruva M, Shim H, Mullins ME. Clinical applications of magnetic resonance spectroscopy in brain tumors: from diagnosis to treatment. Radiol Clin North Am. 2021; 59: 349-62.

12. Maudsley AA, Andronesi OC, Barker PB, Bizzi A, Bogner W, Henning A, et al. Advanced magnetic resonance spectroscopic neuroimaging: experts' consensus recommendations. NMR Biomed. 2021; 34: e4309.

13. Venkataramani V, Tanev DI, Strahle C, Studier-Fischer A, Fankhauser L, Kessler T, et al. Glutamatergic synaptic input to glioma cells drives brain tumour progression. Nature. 2019; 573: 532-8.

14. Lell MM, Kachelrieß M. Recent and upcoming technological developments in computed tomography: high speed, low dose, deep learning, multienergy. Invest Radiol. 2020; 55: 8-19.

15. Li B, Toth TL, Hsieh J, Tang X. Simulation and analysis of image quality impacts from single source, ultra-wide coverage CT scanner. J Xray Sci Technol. 2012; 20: 395-404.

16. Rajiah P, Cummings KW, Williamson E, Young PM. CT fractional flow reserve: a practical guide to application, interpretation, and problem solving. Radiographics. 2022; 42: 340-58.

17. Kirresh A, White L, Mitchell A, Ahmad S, Obika B, Davis S, et al. Radiation-induced coronary artery disease: a difficult clinical conundrum. Clin Med (Lond). 2022; 22: 251-6.

18. Messerli M, Kluckert T, Knitel M, Wälti S, Desbiolles L, Rengier F, et al. Ultralow dose CT for pulmonary nodule detection with chest x-ray equivalent dose - a prospective intra-individual comparative study. Eur Radiol. 2017; 27: 3290-9.

19. Gordic S, Morsbach F, Schmidt B, Allmendinger T, Flohr T, Husarik D, et al. Ultralow-dose chest computed tomography for pulmonary nodule detection: first performance evaluation of single energy scanning with spectral shaping. Invest Radiol. 2014; 49: 465-73.

20. Feuchtner GM, Jodocy D, Klauser A, Haberfellner B, Aglan I, Spoeck A, et al. Radiation dose reduction by using 100-kV tube voltage in cardiac 64-slice computed tomography: a comparative study. Eur J Radiol. 2010; 75: e51-6.

21. Lurz M, Lell MM, Wuest W, Eller A, Scharf M, Uder M, et al. Automated tube voltage selection in thoracoabdominal computed tomography at high pitch using a third-generation dual-source

scanner: image quality and radiation dose performance. Invest Radiol. 2015; 50: 352-60.

22. Hendriks BMF, Eijsvoogel NG, Kok M, Martens B, Wildberger JE, Das M. Optimizing pulmonary embolism computed tomography in the age of individualized medicine: a prospective clinical study. Invest Radiol. 2018; 53: 306-12.

23. Choi HK, Mazzone PJ. Lung cancer screening. Med Clin North Am. 2022; 106: 1041-53.

24. Becker N, Motsch E, Trotter A, Heussel CP, Dienemann H, Schnabel PA, et al. Lung cancer mortality reduction by LDCT screening-results from the randomized German LUSI trial. Int J Cancer. 2020; 146: 1503-13.

25. Nakamura Y, Higaki T, Kondo S, Kawashita I, Takahashi I, Awai K. An introduction to photon-counting detector CT (PCD CT) for radiologists. Jpn J Radiol. 2022. doi: 10.1007/s11604-022-01350-6.

26. Tortora M, Gemini L, D'Iglio I, Ugga L, Spadarella G, Cuocolo R. Spectral photon-counting computed tomography: a review on technical principles and clinical applications. J Imaging. 2022; 8: 112.

27. Klein L, Dorn S, Amato C, Heinze S, Uhrig M, Schlemmer HP, et al. Effects of detector sampling on noise reduction in clinical photon-counting whole-body computed tomography. Invest Radiol. 2020; 55: 111-9.

28. Si-Mohamed S, Tatard-Leitman V, Laugerette A, Sigovan M, Pfeiffer D, Rummeny EJ, et al. Spectral photon-counting computed tomography (SPCCT): in-vivo single-acquisition multi-phase liver imaging with a dual contrast agent protocol. Sci Rep. 2019; 9: 8458.

29. Symons R, Krauss B, Sahbaee P, Cork TE, Lakshmanan MN, Bluemke DA, et al. Photon-counting CT for simultaneous imaging of multiple contrast agents in the abdomen: an in vivo study. Med Phys. 2017; 44: 5120-7.

30. Badea CT, Clark DP, Holbrook M, Srivastava M, Mowery Y, Ghaghada KB. Functional imaging of tumor vasculature using iodine and gadolinium-based nanoparticle contrast agents: a comparison of spectral micro-CT using energy integrating and photon counting detectors. Phys Med Biol. 2019; 64: 065007.

31. Thivolet A, Si-Mohamed S, Bonnot PE, Blanchet C, Képénékian V, Boussel L, et al. Spectral photon-counting CT imaging of colorectal peritoneal metastases: initial experience in rats. Sci Rep. 2020; 10: 13394.

32. Allphin AJ, Mowery YM, Lafata KJ, Clark DP, Bassil AM, Castillo R, et al. Photon counting CT and radiomic analysis enables differentiation of tumors based on lymphocyte burden. Tomography. 2022; 8: 740-53.

33. Wehrse E, Klein L, Rotkopf LT, Stiller W, Finke M, Echner G, et al. Ultrahigh resolution whole body photon counting computed tomography as a novel versatile tool for translational research from mouse to man. Z Med Phys. 2022; S0939-3889(22)00066-6. doi: 10.1016/j.zemedi.2022.06.002.

34. Leng S, Rajendran K, Gong H, Zhou W, Halaweish AF, Henning A, et al. 150-μm spatial resolution using photon-counting detector computed tomography technology: technical performance and first patient images. Invest Radiol. 2018; 53: 655-62.

35. Wetzl M, Wenkel E, Balbach E, Dethlefsen E, Hartmann A, Emons J, et al. Detection of microcalcifications in spiral breast computed tomography with photon-counting detector is feasible: a specimen study. Diagnostics (Basel). 2021; 11: 848.

36. Bartlett DJ, Koo CW, Bartholmai BJ, Rajendran K, Weaver JM, Halaweish AF, et al. High-resolution chest computed tomography imaging of the lungs: impact of 1024 matrix reconstruction and photon-counting detector computed tomography. Invest Radiol. 2019; 54: 129-37.

37. Wehrse E, Sawall S, Klein L, Glemser P, Delorme S, Schlemmer HP, et al. Potential of ultra-high-resolution photon-counting CT of bone metastases: initial experiences in breast cancer patients. NPJ Breast Cancer. 2021; 7: 3.

38. Symons R, Cork TE, Sahbaee P, Fuld MK, Kappler S, Folio LR, et al. Low-dose lung cancer screening with photon-counting CT: a feasibility study. Phys Med Biol. 2017; 62: 202-13.

39. Lee CL, Park J, Nam S, Choi J, Choi Y, Lee S, et al. Metal artifact reduction and tumor detection using photon-counting multi-energy computed tomography. PLoS One. 2021; 16: e0247355.

40. Fukugawa Y, Toya R, Matsuyama T, Watakabe T, Shimohigashi Y, Kai Y, et al. Impact of metal artifact reduction algorithm on gross tumor volume delineation in tonsillar cancer: reducing the interobserver variation. BMC Med Imaging. 2022; 22: 161.

41. Momose A, Takeda T, Itai Y, Hirano K. Phase-contrast X-ray computed tomography for observing biological soft tissues. Nat Med. 1996; 2: 473-5.

42. Walsh CL, Tafforeau P, Wagner WL, Jafree DJ, Bellier A, Werlein C, et al. Imaging intact human organs with local resolution of cellular structures using hierarchical phase-contrast tomography. Nat Methods. 2021; 18: 1532-41.

43. Walsh C, Tafforeau P, Wagner WL, Jafree DJ, Bellier A, Werlein C, et al. Multiscale three-dimensional imaging of intact human organs down to the cellular scale using hierarchical phase-contrast tomography. bioRxiv. 2021. doi: 10.1101/2021.02.03.429481.

44. Graafen D, Müller L, Halfmann M, Düber C, Hahn F, Yang Y, et al. Photon-counting detector CT improves quality of arterial phase abdominal scans: a head-to-head comparison with energy-integrating CT. Eur J Radiol. 2022; 156: 110514.

45. Soschynski M, Hagen F, Baumann S, Hagar MT, Weiss J, Krauss T, et al. High temporal resolution dual-source photon-counting CT for coronary artery disease: initial multicenter clinical experience. J Clin Med. 2022; 11: 6003.

46. Jackson JA, Langham WH. Whole-body NMR spectrometer. Rev Sci Instrum. 1968; 39: 510-3.

47. Damadian R. Tumor detection by nuclear magnetic resonance. Science. 1971; 171: 1151-3.

48. Weisman ID, Bennett LH, Maxwell LR, Woods MW, Burk D. Recognition of cancer in vivo by nuclear magnetic resonance. Science. 1972; 178: 1288-90.

49. Lauterbur PC. Image formation by induced local interactions: examples employing nuclear magnetic resonance. Nature. 1973; 242: 190-1.

50. Brown RW, Cheng YCN, Haacke EM, Thompson MR, Venkatesan R. Magnetic Resonance Imaging: Physical Principles and Sequence Design. John Wiley & Sons Ltd. doi: 10.1002/9781118633953.

51. Bieri O, Scheffler K. Fundamentals of balanced steady state free precession MRI. J Magn Reson Imaging. 2013; 38: 2-11.

52. Messina C, Bignone R, Bruno A, Bruno A, Bruno F, Calandri M, et al. Diffusion-weighted imaging in oncology: an update. Cancers (Basel). 2020; 12: 1493.

53. Schurink NW, Lambregts DMJ, Beets-Tan RGH. Diffusion-weighted imaging in rectal cancer: current applications and future perspectives. Br J Radiol. 2019; 92: 20180655.

54. Tamada T, Ueda Y, Ueno Y, Kojima Y, Kido A, Yamamoto A. Diffusion-weighted imaging in prostate cancer. MAGMA. 2022; 35: 533-47.

55. Baltzer P, Mann RM, Iima M, Sigmund EE, Clauser P, Gilbert FJ, et al. Diffusion-weighted imaging of the breast-a consensus and mission statement from the EUSOBI International Breast Diffusion-Weighted Imaging working group. Eur Radiol. 2020; 30: 1436-50.

56. De Robertis R, Tinazzi Martini P, Demozzi E, Dal Corso F, Bassi C, Pederzoli P, et al. Diffusion-weighted imaging of pancreatic cancer. World J Radiol. 2015; 7: 319-28.

57. Connolly M, Srinivasan A. Diffusion-weighted imaging in head and neck cancer: technique, limitations, and applications. Magn Reson Imaging Clin N Am. 2018; 26: 121-33.

58. Gupta RT, Mehta KA, Turkbey B, Verma S. PI-RADS: past, present, and future. J Magn Reson Imaging. 2020; 52: 33-53.

59. Spak DA, Plaxco JS, Santiago L, Dryden MJ, Dogan BE. BI-RADS® fifth edition: a summary of changes. Diagn Interv Imaging. 2017; 98: 179-90.

60. Messiou C, Hillengass J, Delorme S, Lecouvet FE, Moulopoulos LA, Collins DJ, et al. Guidelines for acquisition, interpretation, and reporting of whole-body MRI in myeloma: myeloma response assessment and diagnosis system (MY-RADS). Radiology. 2019; 291: 5-13.

61. Thomassin-Naggara I, Poncelet E, Jalaguier-Coudray A, Guerra A, Fournier LS, Stojanovic S, et al. Ovarian-Adnexal Reporting Data System Magnetic Resonance Imaging (O-RADS MRI) score for risk stratification of sonographically indeterminate adnexal masses. JAMA Netw Open. 2020; 3: e1919896.

62. Petralia G, Zugni F, Summers PE, Colombo A, Pricolo P, Grazioli L, et al. Whole-body magnetic resonance imaging (WB-MRI) for cancer screening: recommendations for use. Radiol Med. 2021; 126: 1434-50.

63. Partovi S, Sin D, Lu Z, Sieck L, Marshall H, Pham R, et al. Fast MRI breast cancer screening - ready for prime time. Clin Imaging. 2020; 60: 160-8.

64. Biederer J, Ohno Y, Hatabu H, Schiebler ML, van Beek EJR, Vogel-Claussen J, et al. Screening for lung cancer: does MRI have a role? Eur J Radiol. 2017; 86: 353-60.

65. Eldred-Evans D, Tam H, Sokhi H, Padhani AR, Winkler M, Ahmed HU. Rethinking prostate cancer screening: could MRI be an alternative screening test? Nat Rev Urol. 2020; 17: 526-39.

1580

Kurz and Schlemmer. Imaging in translational cancer research

66. Lerner A, Mogensen MA, Kim PE, Shiroishi MS, Hwang DH, Law M. Clinical applications of diffusion tensor imaging. World Neurosurg. 2014; 82: 96-109.

67. Jende JME, Kender Z, Mooshage C, Groener JB, Alvarez-Ramos L, Kollmer J, et al. Diffusion tensor imaging of the sciatic nerve as a surrogate marker for nerve functionality of the upper and lower limb in patients with diabetes and prediabetes. Front Neurosci. 2021; 15: 642589.

68. Li Y, Zhang W. Quantitative evaluation of diffusion tensor imaging for clinical management of glioma. Neurosurg Rev. 2020; 43: 881-91.

69. Yamada I, Yohino N, Yokokawa M, Oikawa Y, Harada H, Hikishima K, et al. Diffusion tensor imaging of oral carcinoma: clinical evaluation and comparison with histopathological findings. Magn Reson Imaging. 2021; 77: 99-108.

70. Bilgin SS, Gultekin MA, Yurtsever I, Yilmaz TF, Cesme DH, Bilgin M, et al. Diffusion tensor imaging can discriminate the primary cell type of intracranial metastases for patients with lung cancer. Magn Reson Med Sci. 2022; 21: 425-31.

71. Tian W, Zhang J, Tian F, Shen J, Niu T, He G, et al. Correlation of diffusion tensor imaging parameters and Gleason scores of prostate cancer. Exp Ther Med. 2018; 15: 351-6.

72. Lin TT, Li XX, Lv WF, Dong JN, Wei C, Wang TT, et al. Diagnostic value of combined intravoxel incoherent motion diffusion-weighted magnetic resonance imaging with diffusion tensor imaging in predicting parametrial infiltration in cervical cancer. Contrast Media Mol Imaging. 2021; 2021: 6651070.

73. Iima M, Le Bihan D. Clinical intravoxel incoherent motion and diffusion MR imaging: past, present, and future. Radiology. 2016; 278: 13-32.

74. Federau C. Intravoxel incoherent motion MRI as a means to measure in vivo perfusion: a review of the evidence. NMR Biomed. 2017; 30.

75. Iima M. Perfusion-driven intravoxel incoherent motion (IVIM) MRI in oncology: applications, challenges, and future trends. Magn Reson Med Sci. 2021; 20: 125-38.

76. Zhou Y, Zheng J, Yang C, Peng J, Liu N, Yang L, et al. Application of intravoxel incoherent motion diffusion-weighted imaging in hepatocellular carcinoma. World J Gastroenterol. 2022; 28: 3334-45.

77. Zhang YD, Wang Q, Wu CJ, Wang XN, Zhang J, Liu H, et al. The histogram analysis of diffusion-weighted intravoxel incoherent motion (IVIM) imaging for differentiating the gleason grade of prostate cancer. Eur Radiol. 2015; 25: 994-1004.

78. Iima M, Kataoka M, Kanao S, Onishi N, Kawai M, Ohashi A, et al. Intravoxel incoherent motion and quantitative non-Gaussian diffusion MR imaging: evaluation of the diagnostic and prognostic value of several markers of malignant and benign breast lesions. Radiology. 2018; 287: 432-41.

79. Haller S, Haacke EM, Thurnher MM, Barkhof F. Susceptibility-weighted imaging: technical essentials and clinical neurologic applications. Radiology. 2021; 299: 3-26.

80. Kurz FT, Freitag M, Schlemmer HP, Bendszus M, Ziener CH. Grundlagen und Anwendungen der suszeptibilitätsgewichteten Bildgebung. Radiologe. 2016; 56: 124-36.

81. Hsu CCT, Watkins TW, Kwan GNC, Haacke EM. Susceptibility-weighted imaging of glioma: update on current imaging status and future directions. J Neuroimaging. 2016; 26: 383-90.

82. Gaudino S, Marziali G, Pezzullo G, Guadalupi P, Giordano C, Infante A, et al. Role of susceptibility-weighted imaging and intratumoral susceptibility signals in grading and differentiating pediatric brain tumors at 1.5 T: a preliminary study. Neuroradiology. 2020; 62: 705-13.

83. Schwarz D, Niederle T, Münch P, Hielscher T, Hassel JC, Schlemmer HP, et al. Susceptibility-weighted imaging in malignant melanoma brain metastasis. J Magn Reson Imaging. 2019; 50: 1251-9.

84. Böker SM, Adams LC, Bender YY, Fahlenkamp UL, Wagner M, Hamm B, et al. Differentiation of predominantly osteoblastic and osteolytic spine metastases by using susceptibility-weighted MRI. Radiology. 2019; 290: 146-54.

85. Takeuchi M, Matsuzaki K, Harada M. Clinical utility of susceptibility-weighted MR sequence for the evaluation of uterine sarcomas. Clin Imaging. 2019; 53: 143-50.

86. Alonzi R, Taylor NJ, Stirling JJ, d'Arcy JA, Collins DJ, Saunders MI, et al. Reproducibility and correlation between quantitative and semiquantitative dynamic and intrinsic susceptibility-weighted MRI parameters in the benign and malignant human prostate. J Magn Reson Imaging. 2010; 32: 155-64.

87. Vinayagamani S, Sheelakumari R, Sabarish S, Senthilvelan S, Ros R, Thomas B, et al. Quantitative susceptibility mapping: technical considerations and clinical applications in neuroimaging. J Magn Reson Imaging. 2021; 53: 23-37.

88. Buschle LR, Kampf T, Kurz FT, Sturm VJF, Pham M, Schlemmer HP, et al. Voxel-size dependent quantitative susceptibility mapping of blood vessel networks: a simulation study. Z Med Phys. 2019; 29: 282-91.

89. Reith TP, Prah MA, Choi EJ, Lee J, Wujek R, Al-Gizawiy M, et al. Basal ganglia iron content increases with glioma severity using quantitative susceptibility mapping: a potential biomarker of tumor severity. Tomography. 2022; 8: 789-97.

90. Taylor AJ, Salerno M, Dharmakumar R, Jerosch-Herold M. T1 mapping: basic techniques and clinical applications. JACC Cardiovasc Imaging. 2016; 9: 67-81.

91. O'Brien AT, Gil KE, Varghese J, Simonetti OP, Zareba KM. T2 mapping in myocardial disease: a comprehensive review. J Cardiovasc Magn Reson. 2022; 24: 33.

92. Menacho K, Abdel-Gadir A, Moon JC, Fernandes JL. T2* mapping techniques: iron overload assessment and other potential clinical applications. Magn Reson Imaging Clin N Am. 2019; 27: 439-51.

93. Jeong D, Patel A, Francois CJ, Gage KL, Fradley MG. Cardiac magnetic resonance imaging in oncology. Cancer Control. 2017; 24: 147-60.

94. Auer TA, Kern M, Fehrenbach U, Tanyldizi Y, Misch M, Wiener E. T2 mapping of the peritumoral infiltration zone of glioblastoma and anaplastic astrocytoma. Neuroradiol J. 2021; 34: 392-400.

95. Jiang J, Cui L, Xiao Y, Zhou X, Fu Y, Xu G, et al. B_1-corrected T1 mapping in lung cancer: repeatability, reproducibility, and identification of histological types. J Magn Reson Imaging. 2021; 54: 1529-40.

96. Makowski MR, Bressem KK, Franz L, Kader A, Niehues SM, Keller S, et al. De novo radiomics approach using image augmentation and features from T1 mapping to predict gleason scores in prostate cancer. Invest Radiol. 2021; 56: 661-8.

97. Mai J, Abubrig M, Lehmann T, Hilbert T, Weiland E, Grimm MO, et al. T2 mapping in prostate cancer. Invest Radiol. 2019; 54: 146-52.

98. Mann RM, Cho N, Moy L. Breast MRI: state of the art. Radiology. 2019; 292: 520-36.

99. Stabile A, Giganti F, Rosenkrantz AB, Taneja SS, Villeirs G, Gill IS, et al. Multiparametric MRI for prostate cancer diagnosis: current status and future directions. Nat Rev Urol. 2020; 17: 41-61.

100. Thomaides-Brears HB, Lepe R, Banerjee R, Duncker C. Multiparametric MR mapping in clinical decision-making for diffuse liver disease. Abdom Radiol (NY). 2020; 45: 3507-22.

101. Gao W, Yang Q, Li X, Chen X, Wei X, Diao Y, et al. Synthetic MRI with quantitative mappings for identifying receptor status, proliferation rate, and molecular subtypes of breast cancer. Eur J Radiol. 2022; 148: 110168.

102. Du S, Gao S, Zhao R, Liu H, Wang Y, Qi X, et al. Contrast-free MRI quantitative parameters for early prediction of pathological response to neoadjuvant chemotherapy in breast cancer. Eur Radiol. 2022; 32: 5759-72.

103. Klingebiel M, Schimmöller L, Weiland E, Franiel T, Jannusch K, Kirchner J, et al. Value of T2 mapping MRI for prostate cancer detection and classification. J Magn Reson Imaging. 2022; 56: 413-22.

104. Hepp T, Kalmbach L, Kolb M, Martirosian P, Hilbert T, Thaiss WM, et al. T2 mapping for the characterization of prostate lesions. World J Urol. 2022; 40: 1455-61.

105. Poker A, Karcaaltıncaba M, Ozmen MN, Karaosmanoğlu AD, Erdemir AG, Ocal O, et al. Multiparametric MRI with MR elastography findings in patients with sinusoidal obstruction syndrome after oxaliplatin-based chemotherapy. Insights Imaging. 2022; 13: 147.

106. Cieszanowski A, Anysz-Grodzicka A, Szeszkowski W, Kaczynski B, Maj E, Gornicka B, et al. Characterization of focal liver lesions using quantitative techniques: comparison of apparent diffusion coefficient values and T2 relaxation times. Eur Radiol. 2012; 22: 2514-24.

107. Keller S, Borde T, Brangsch J, Adams LC, Kader A, Reimann C, et al. Native T1 mapping magnetic resonance imaging as a quantitative biomarker for characterization of the extracellular matrix in a rabbit hepatic cancer model. Biomedicines. 2020; 8: 412.

108. Faller TL, Trotier AJ, Miraux S, Ribot EJ. Radial MP2RAGE sequence for rapid 3D T1 mapping of mouse abdomen: application to hepatic metastases. Eur Radiol. 2019; 29: 5844-51.

109. Calamante F. Perfusion MRI using dynamic-susceptibility contrast MRI: quantification issues in patient studies. Top Magn Reson Imaging. 2010; 21: 75-85.

110. Quan G, Zhang K, Liu Y, Ren JL, Huang D, Wang W, et al. Role of dynamic susceptibility contrast perfusion MRI in glioma progression evaluation. J Oncol. 2021; 2021: 1696387.

111. Boxerman JL, Quarles CC, Hu LS, Erickson BJ, Gerstner ER, Smits M, et al. Consensus recommendations for a dynamic susceptibility contrast MRI protocol for use in high-grade gliomas. Neuro Oncol. 2020; 22: 1262-75.

112. Bian Y, Jin P, Wang Y, Wei X, Qiang Y, Niu G, et al. Clinical applications of DSC-MRI parameters assess angiogenesis and differentiate malignant from benign soft tissue tumors in limbs. Acad Radiol. 2020; 27: 354-60.

113. Abdel Razek AAK, Samir S, Ashmalla GA. Characterization of parotid tumors with dynamic susceptibility contrast perfusion-weighted magnetic resonance imaging and diffusion-weighted MR imaging. J Comput Assist Tomogr. 2017; 41: 131-36.

114. Razek AAKA, Elsorogy LG, Soliman NY, Nada N. Dynamic susceptibility contrast perfusion MR imaging in distinguishing malignant from benign head and neck tumors: a pilot study. Eur J Radiol. 2011; 77: 73-9.

115. Petralia G, Summers PE, Agostini A, Ambrosini R, Cianci R, Cristel G, et al. Dynamic contrast-enhanced MRI in oncology: how we do it. Radiol Med. 2020; 125: 1288-300.

116. Tofts PS, Brix G, Buckley DL, Evelhoch JL, Henderson E, Knopp MV, et al. Estimating kinetic parameters from dynamic contrast-enhanced T(1)-weighted MRI of a diffusable tracer: standardized quantities and symbols. J Magn Reson Imaging. 1999; 10: 223-32.

117. Kim R, Choi SH, Yun TJ, Lee ST, Park CK, Kim TM, et al. Prognosis prediction of non-enhancing T2 high signal intensity lesions in glioblastoma patients after standard treatment: application of dynamic contrast-enhanced MR imaging. Eur Radiol. 2017; 27: 1176-85.

118. Do RKG, Rusinek H, Taouli B. Dynamic contrast-enhanced MR imaging of the liver: current status and future directions. Magn Reson Imaging Clin N Am. 2009; 17: 339-49.

119. Kabadi SJ, Fatterpekar GM, Anzai Y, Mogen J, Hagiwara M, Patel SH. Dynamic contrast-enhanced MR imaging in head and neck cancer. Magn Reson Imaging Clin N Am. 2018; 26: 135-49.

120. Pauling L, Coryell CD. The magnetic properties and structure of hemoglobin, oxyhemoglobin and carbonmonoxyhemoglobin. Proc Natl Acad Sci U S A. 1936; 22: 210-6.

121. Ogawa S, Lee TM, Kay AR, Tank DW. Brain magnetic resonance imaging with contrast dependent on blood oxygenation. Proc Natl Acad Sci U S A. 1990; 87: 9868-72.

122. Haller S, Bartsch AJ. Pitfalls in FMRI. Eur Radiol. 2009; 19: 2689-706.

123. Lyon L. Dead salmon and voodoo correlations: should we be sceptical about functional MRI? Brain. 2017; 140: e53.

124. Padhani AR, Krohn KA, Lewis JS, Alber M. Imaging oxygenation of human tumours. Eur Radiol. 2007; 17: 861-72.

125. O'Connor JPB, Robinson SP, Waterton JC. Imaging tumour hypoxia with oxygen-enhanced MRI and BOLD MRI. Br J Radiol. 2019; 92: 20180642.

126. Hallac RR, Zhou H, Pidikiti R, Song K, Stojadinovic S, Zhao D, et al. Correlations of noninvasive BOLD and TOLD MRI with pO2 and relevance to tumor radiation response. Magn Reson Med. 2014; 71: 1863-73.

1582

Kurz and Schlemmer. Imaging in translational cancer research

127. O'Connor JPB, Boult JK, Jamin Y, Babur M, Finegan KG, Williams KJ, et al. Oxygen-enhanced MRI accurately identifies, quantifies, and maps tumor hypoxia in preclinical cancer models. Cancer Res. 2016; 76: 787-95.

128. Duan L, Huang H, Sun F, Zhao Z, Wang M, Xing M, et al. Comparing the blood oxygen level-dependent fluctuation power of benign and malignant musculoskeletal tumors using functional magnetic resonance imaging. Front Oncol. 2022; 12: 794555.

129. Cai S, Shi Z, Zhou S, Liang Y, Wang L, Wang K, et al. Cerebrovascular dysregulation in patients with glioma assessed with time-shifted BOLD fMRI. Radiology. 2022; 304: 155-63.

130. Bunevicius A, Schregel K, Sinkus R, Golby A, Patz S. Review: MR elastography of brain tumors. Neuroimage Clin. 2020; 25: 102109.

131. Manduca A, Bayly PJ, Ehman RL, Kolipaka A, Royston TJ, Sack I, et al. MR elastography: principles, guidelines, and terminology. Magn Reson Med. 2021; 85: 2377-90.

132. Patel BK, Samreen N, Zhou Y, Chen J, Brandt K, Ehman R, et al. MR elastography of the breast: evolution of technique, case examples, and future directions. Clin Breast Cancer. 2021; 21: e102-11.

133. Idilman IS, Li J, Yin M, Venkatesh SK. MR elastography of liver: current status and future perspectives. Abdom Radiol (NY). 2020; 45: 3444-62.

134. Vogl TJ, Dosch MP, Haas Y. MR elastography is a good response parameter for microwave ablation liver tumors. Eur J Radiol. 2022; 152: 110360.

135. Cho HJ, Kim B, Kim HJ, Huh J, Kim JK, Lee JH, et al. Liver stiffness measured by MR elastography is a predictor of early HCC recurrence after treatment. Eur Radiol. 2020; 30: 4182-92.

136. Fovargue D, Fiorito M, Capilnasiu A, Nordsletten D, Lee J, Sinkus R, et al. Towards noninvasive estimation of tumour pressure by utilising MR elastography and nonlinear biomechanical models: a simulation and phantom study. Sci Rep. 2020; 10: 5588.

137. Reiter R. Majumdar S, Kearney S, Kajdacsy-Balla A, Macias V, Crivellaro S, et al. Investigating the heterogeneity of viscoelastic properties in prostate cancer using MR elastography at 9.4 T in fresh prostatectomy specimens. Magn Reson Imaging. 2022; 87: 113-8.

138. Ho ML. Arterial spin labeling: clinical applications. J Neuroradiol. 2018; 45: 276-89.

139. Troudi A, Tensaouti F, Baudou E, Péran P, Laprie A. Arterial spin labeling perfusion in pediatric brain tumors: a review of techniques, quality control, and quantification. Cancers (Basel). 2022; 14: 4734.

140. Abdel Razek AAK, Talaat M, El-Serougy L, Gaballa G, Abdelsalam M. Clinical applications of arterial spin labeling in brain tumors. J Comput Assist Tomogr. 2019; 43: 525-32.

141. Tanaka F, Umino M, Maeda M, Nakayama R, Inoue K, Kogue R, et al. Pseudocontinuous arterial spin labeling: clinical applications and usefulness in head and neck entities. Cancers (Basel). 2022; 14: 3872.

142. Zhang K, Sturm VJ, Buschle LR, Hahn A, Yun SD, Jon Shah N, et al. Dual-contrast pCASL using simultaneous gradient-echo/spin-echo multiband EPI. Magn Reson Imaging. 2019; 57: 359-67.

143. Zhang HM, Wen DG, Wang Y, Bao YG, Yuan Y, Chen YT, et al. Arterial spin labeling MRI for predicting microvascular invasion of T1 staging renal clear cell carcinoma preoperatively. Front Oncol. 2021; 11: 644975.

144. Martirosian P, Pohmann R, Schraml C, Schwartz M, Kuestner T, Schwenzer NF, et al. Spatial-temporal perfusion patterns of the human liver assessed by pseudo-continuous arterial spin labeling MRI. Z Med Phys. 2019; 29: 173-83.

145. Aramendía-Vidaurreta V, Gordaliza PM, Vidorreta M, Echeverría-Chasco R, Bastarrika G, Muñoz-Barrutia A, et al. Reduction of motion effects in myocardial arterial spin labeling. Magn Reson Med. 2022; 87: 1261-75.

146. Diaz de Leon A, Costa D, Pedrosa I. Role of multiparametric MR imaging in malignancies of the urogenital tract. Magn Reson Imaging Clin N Am. 2016; 24: 187-204.

147. Kim KH, Choi SH, Park SH. Improving arterial spin labeling by using deep learning. Radiology. 2018; 287: 658-66.

148. Payne GS. Clinical applications of in vivo magnetic resonance spectroscopy in oncology. Phys Med Biol. 2018; 63: 21TR02.

149. Brandão LA, Castillo M. Adult brain tumors: clinical applications of magnetic resonance spectroscopy. Magn Reson Imaging Clin N Am. 2016; 24: 781-809.

150. Sharma U, Jagannathan NR. Metabolism of prostate cancer by magnetic resonance spectroscopy (MRS). Biophys Rev. 2020; 12: 1163-73.

151. Zeinali-Rafsanjani B, Jalli R, Saeedi-Moghadam M, Pishdad P. Magnetic resonance spectroscopy and its application in colorectal cancer diagnosis and screening: a narrative review. J Med Imaging Radiat Sci. 2020; 51: 654-61.

152. Fujima N, Carlota Andreu-Arasa V, Barest GD, Srinivasan A, Sakai O. Magnetic resonance spectroscopy of the head and neck: principles, applications, and challenges. Neuroimaging Clin N Am. 2020; 30: 283-93.

153. Jagannathan NR, Sharma U. Breast tissue metabolism by magnetic resonance spectroscopy. Metabolites. 2017; 7: 25.

154. Jiang S, Wen Z, Ahn SS, Cai K, Paech D, Eberhart CG, et al. Applications of chemical exchange saturation transfer magnetic resonance imaging in identifying genetic markers in gliomas. NMR Biomed. 2022; e4731. doi: 10.1002/nbm.4731.

155. Igarashi T, Kim H, Sun PZ. Detection of tissue pH with quantitative chemical exchange saturation transfer magnetic resonance imaging. NMR Biomed. 2022; e4711. doi: 10.1002/nbm.4711.

156. Dou W, Lin CE, Ding H, Shen Y, Dou C, Qian L, et al. Chemical exchange saturation transfer magnetic resonance imaging and its main and potential applications in pre-clinical and clinical studies. Quant Imaging Med Surg. 2019; 9: 1747-66.

157. Seidemo A, Lehmann PM, Rydhög A, Wirestam R, Helms G, Zhang Y, et al. Towards robust glucose chemical exchange saturation transfer imaging in humans at 3 T: arterial input function measurements and the effects of infusion time. NMR Biomed. 2022; 35: e4624.

158. Wang L, Zhou Z, Gaddam S, Wang N, Xie Y, Deng Z, et al. Chemical exchange saturation transfer for pancreatic ductal adenocarcinoma evaluation. Pancreas. 2022; 51: 463-8.

159. Kim H, Wu Y, Villano D, Longo DL, McMahon MT, Sun PZ. Analysis protocol for the quantification of renal pH using chemical exchange saturation transfer (CEST) MRI. Methods Mol Biol. 2021; 2216: 667-88.

160. Evans VS, Torrealdea F, Rega M, Brizmohun Appayya M, Latifoltojar A, Sidhu H, et al. Optimization and repeatability of multipool chemical exchange saturation transfer MRI of the prostate at 3.0 T. J Magn Reson Imaging. 2019; 50: 1238-50.

161. Rivlin M, Anaby D, Nissan N, Zaiss M, Deshmane A, Navon G, et al. Breast cancer imaging with glucosamine CEST (chemical exchange saturation transfer) MRI: first human experience. Eur Radiol. 2022. doi: 10.1007/s00330-022-08772-w.

162. Jeong D, Gladish G, Chitiboi T, Fradley MG, Gage KL, Schiebler ML. MRI in cardio-oncology: a review of cardiac complications in oncologic care. J Magn Reson Imaging. 2019; 50: 1349-66.

163. Biersmith MA, Tong MS, Guha A, Simonetti OP, Addison D. Multimodality cardiac imaging in the era of emerging cancer therapies. J Am Heart Assoc. 2020; 9: e013755.

164. Ginat DT, Fong MW, Tuttle DJ, Hobbs SK, Vyas RC. Cardiac imaging: part 1, MR pulse sequences, imaging planes, and basic anatomy. AJR Am J Roentgenol. 2011; 197: 808-15.

165. Eyre K, Lindsay K, Razzaq S, Chetrit M, Friedrich M. Simultaneous multi-parametric acquisition and reconstruction techniques in cardiac magnetic resonance imaging: basic concepts and status of clinical development. Front Cardiovasc Med. 2022; 9: 953823.

166. Buckley O, Madan R, Kwong R, Rybicki FJ, Hunsaker A. Cardiac masses, part 1: imaging strategies and technical considerations. AJR Am J Roentgenol. 2011; 197: W837-41.

167. Yang Q, LI Q, Liu X, Du X, Bi X, Huang F, et al. 3.0T whole-heart coronary magnetic resonance angiography performed with 32-channel cardiac coils: a single center experience. Circ Cardiovasc Imaging. 2012; 5: 573-9.

168. de Malherbe M, Duhamel A, Tacelli N, Hachulla AL, Pontana F, Faivre JB, et al. Ultrafast imaging of the entire chest without ECG synchronisation or beta-blockade: to what extent can we analyse the coronary arteries? Insights Imaging. 2012; 3: 73-9.

169. Goyen M, Laub G, Ladd ME, Debatin JF, Barkhausen J, Truemmler KH, et al. Dynamic 3D MR angiography of the pulmonary arteries in under four seconds. J Magn Reson Imaging. 2001; 13: 372-7.

170. Dyverfeldt P, Bissell M, Barker AJ, Bolger AF, Carlhäll CJ, Ebbers T, et al. 4D flow cardiovascular magnetic resonance consensus statement. J Cardiovasc Magn Reson. 2015; 17: 72.

171. Mabudian L, Jordan JH, Bottinor W, Hundley WG. Cardiac MRI assessment of anthracycline-induced cardiotoxicity. Front Cardiovasc Med. 2022; 9: 903719.

172. Wei X, Lin L, Zhang G, Zhou X. Cardiovascular magnetic resonance imaging in the early detection of cardiotoxicity induced by cancer therapies. Diagnostics (Basel). 2022; 12: 1846.

173. Yablonskiy DA, Haacke EM. Theory of NMR signal behavior in magnetically inhomogeneous tissues: the static dephasing regime. Magn Reson Med. 1994; 32: 749-63.

174. Kurz FT, Kampf T, Heiland S, Bendszus M, Schlemmer HP, Ziener CH. Theoretical model of the single spin-echo relaxation time for spherical magnetic perturbers. Magnetic Reson Med. 2014; 71: 1888-95.

175. Kurz FT, Ziener CH, Rückl M, Hahn A, Sturm VJF, Zhang K, et al. The influence of spatial patterns of capillary networks on transverse relaxation. Magn Reson Imaging. 2017; 40: 31-47.

176. Jensen JH, Chandra R. NMR relaxation in tissues with weak magnetic inhomogeneities. Magn Reson Med. 2000; 44: 144-56.

177. Kiselev VG, Posse S. Analytical theory of susceptibility induced NMR signal dephasing in a cerebrovascular network. Phys Rev Lett. 1998; 81: 5696-9.

178. Bauer WR, Nadler W. Spin dephasing in the extended strong collision approximation. Phys Rev E Stat Nonlin Soft Matter Phys. 2002; 65: 066123.

179. Sukstanskii AL, Yablonskiy DA. Gaussian approximation in the theory of MR signal formation in the presence of structure-specific magnetic field inhomogeneities. J Magn Reson. 2003; 163: 236-47.

180. Kurz FT, Kampf T, Buschle LR, Heiland S, Schlemmer HP, Bendszus M, et al. CPMG relaxation rate dispersion in dipole fields around capillaries. Magn Reson Imaging. 2016; 34: 875-88.

181. Kurz FT, Buschle LR, Kampf T, Zhang K, Schlemmer HP, Heiland S, et al. Spin dephasing in a magnetic dipole field around large capillaries: approximative and exact results. J Magn Reson. 2016; 273: 83-97.

182. Buschle LR, Ziener CH, Zhang K, Sturm VJF, Kampf T, Hahn A, et al. Vessel radius mapping in an extended model of transverse relaxation. MAGMA. 2018; 31: 531-51.

183. Kurz FT, Kampf T, Buschle LR, Schlemmer HP, Bendszus M, Heiland S, et al. Generalized moment analysis of magnetic field correlations for accumulations of spherical and cylindrical magnetic perturbers. Front Phys. 2016; 4: 46.

184. Weiskopf N, Mohammadi S, Lutti A, Callaghan MF. Advances in MRI-based computational neuroanatomy: from morphometry to in-vivo histology. Curr Opin Neurol. 2015; 28: 313-22.

185. Hahn A, Bode J, Schuhegger S, Krüwel T, Sturm VJF, Zhang K, et al. Brain tumor classification of virtual NMR voxels based on realistic blood vessel-induced spin dephasing using support vector machines. NMR Biomed. 2020; 35: e4307.

186. Hahn A, Bode J, Krüwel T, Solecki G, Heiland S, Bendszus M, et al. Glioblastoma multiforme restructures the topological connectivity of cerebrovascular networks. Sci Rep. 2019; 9: 11757.

187. Hahn A, Bode J, Krüwel T, Kampf T, Buschle LR, Sturm VJF, et al. Gibbs point field model quantifies disorder in microvasculature of U87-glioblastoma. J Theor Biol. 2020; 494: 110230.

188. Sukstanskii AL, Yablonskiy DA. On the role of neuronal magnetic susceptibility and structure symmetry on gradient echo MR signal formation. Magn Reson Med. 2014; 71: 345-53.

189. Kurz FT, Buschle LR, Hahn A, Jende JME, Bendszus M, Heiland S, et al. Diffusion effects in myelin sheath free induction decay. J Magn Reson. 2018; 297: 61-75.

190. Jespersen SN, Bjarkam CR, Nyengaard JR, Chakravarty MM, Hansen B, Vosegaard T, et al. Neurite density from magnetic resonance diffusion measurements at ultrahigh field: comparison with light microscopy and electron microscopy. Neuroimage. 2010; 49: 205-16.

1584

Kurz and Schlemmer. Imaging in translational cancer research

191. Novikov DS, Reisert M, Kiselev VG. Effects of mesoscopic susceptibility and transverse relaxation on diffusion NMR. J Magn Reson. 2018; 293: 134-44.

192. Rydhög A, Pasternak O, Ståhlberg F, Ahlgren A, Knutsson L, Wirestam R. Estimation of diffusion, perfusion and fractional volumes using a multi-compartment relaxation-compensated intravoxel incoherent motion (IVIM)signal model. Eur J Radiol Open. 2019; 6: 198-205.

193. Veraart J, Nunes D, Rudrapatna U, Fieremans E, Jones DK, Novikov DS, et al. Noninvasive quantification of axon radii using diffusion MRI. eLife. 2020; 9: e49855.

194. Farrar CT, Kamoun WS, Ley CD, Kim YR, Kwon SJ, Dai G, et al. In vivo validation of MRI vessel caliber index measurement methods with intravital optical microscopy in a U87 mouse brain tumor model. Neuro Oncol. 2010; 12: 341-50.

195. Troprès I, Pannetier N, Grand S, Lemasson B, Moisan A, Péoc'h M, et al. Imaging the microvessel caliber and density: principles and applications of microvascular MRI. Magn Reson Med. 2015; 73: 325-41.

196. Zhang K, Yun SD, Triphan SMF, Sturm VJ, Buschle LR, Hahn A, et al. Vessel architecture imaging using multiband gradient-echo/spin-echo EPI. PLoS ONE. 2019; 14: e0220939.

197. Emblem KE, Mouridsen K, Bjornerud A, Farrar CT, Jennings D, Borra RJ, et al. Vessel architectural imaging identifies cancer patient responders to anti-angiogenic therapy. Nat Med. 2013; 19: 1178-83.

198. Fletcher JW, Djulbegovic B, Soares HP, Siegel BA, Lowe VJ, Lyman GH, et al. Recommendations on the use of 18F-FDG PET in oncology. J Nucl Med. 2008; 49: 480-508.

199. Jin C, Luo X, Li X, Zhou R, Zhong Y, Xu Z, et al. Positron emission tomography molecular imaging-based cancer phenotyping. Cancer. 2022; 128: 2704-16.

200. Mulé S, Reizine E, Blanc-Durand P, Baranes L, Zerbib P, Burns R, et al. Whole-body functional MRI and PET/MRI in multiple myeloma. Cancers (Basel). 2020; 12: 3155.

201. Cheson BD, Fisher RI, Barrington SF, Cavalli F, Schwartz LH, Zucca E, et al. Recommendations for initial evaluation, staging, and response assessment of Hodgkin and non-Hodgkin lymphoma: the Lugano classification. J Clin Oncol. 2014; 32: 3059-68.

202. Tilly H, Gomes da Silva M, Vitolo U, Jack A, Meignan M, Lopez-Guillermo A, et al. Diffuse large B-cell lymphoma (DLBCL): ESMO Clinical Practice Guidelines for diagnosis, treatment and follow-up. Ann Oncol. 2015; 26(Suppl 5): v116-25.

203. Kandathil A, Kay FU, Butt YM, Wachsmann JW, Subramaniam RM. Role of FDG PET/CT in the eighth edition of TNM staging of non-small cell lung cancer. Radiographics. 2018; 38: 2134-49.

204. Hicks RJ, Iravani A, Sandhu S. ^{18}F-fluorodeoxyglucose positron emission tomography/computed tomography for assessing tumor response to immunotherapy in solid tumors: melanoma and beyond. PET Clin. 2020; 15: 11-22.

205. Li YJ, Dai YL, Cheng YS, Zhang WB, Tu CQ. Positron emission tomography (18)F-fluorodeoxyglucose uptake and prognosis in patients with bone and soft tissue sarcoma: a meta-analysis. Eur J Surg Oncol. 2016; 42: 1103-14.

206. Agrawal A, Rangarajan V. Appropriateness criteria of FDG PET/CT in oncology. Indian J Radiol Imaging. 2015; 25: 88-101.

207. Nakamoto Y, Kitajima K, Toriihara A, Nakajo M, Hirata K. Recent topics of the clinical utility of PET/MRI in oncology and neuroscience. Ann Nucl Med. 2022; 36: 798-803.

208. Catalano OA, Lee SI, Parente C, Cauley C, Furtado FS, Striar R, et al. Improving staging of rectal cancer in the pelvis: the role of PET/MRI. Eur J Nucl Med Mol Imaging. 2021; 48: 1235-45.

209. Morawitz J, Bruckmann NM, Dietzel F, Ullrich T, Bittner AK, Hoffmann O, et al. Comparison of nodal staging between CT, MRI, and [18F]-FDG PET/MRI in patients with newly diagnosed breast cancer. Eur J Nucl Med Mol Imaging. 2022; 49: 992-1001.

210. Veldhuijzen van Zanten SEM, Pieterman KJ, Wijnhoven BPL, Pruis I, Koerkamp BG, van Driel LMJW, et al. FAPI PET versus FDG PET, CT or MRI for staging pancreatic-, gastric- and cholangiocarcinoma: systematic review and head-to-head comparisons of diagnostic performances. Diagnostics (Basel). 2022; 12: 1958.

211. Bauckneht M, Albano D, Annunziata S, Santo G, Guglielmo P, Frantellizzi V, et al. Somatostatin receptor PET/CT imaging for the detection and staging of pancreatic NET: a systematic review and meta-analysis. Diagnostics (Basel). 2020; 10: 598.

212. Chen Cardenas SM, Santhanam P. ^{11}C-metomidate PET in the diagnosis of adrenal masses and primary aldosteronism: a review of the literature. Endocrine. 2020; 70: 479-87.

213. Bera K, Braman N, Gupta A, Velcheti V, Madabhushi A. Predicting cancer outcomes with radiomics and artificial intelligence in radiology. Nat Rev Clin Oncol. 2022; 19: 132-46.

214. Ursuleanu TF, Luca AR, Gheorghe L, Grigorovici R, Iancu S, Hlusneac M, et al. Deep learning application for analyzing of constituents and their correlations in the interpretations of medical images. Diagnostics (Basel). 2021; 11: 1373.

215. Ibrahim A, Primakov S, Beuque M, Woodruff HC, Halilaj I, Wu G, et al. Radiomics for precision medicine: current challenges, future prospects, and the proposal of a new framework. Methods. 2021; 188: 20-9.

216. Aftab K, Aamir FB, Mallick S, Mubarak F, Pope WB, Mikkelsen T, et al. Radiomics for precision medicine in glioblastoma. J Neurooncol. 2022; 156: 217-31.

217. Guiot J, Vaidyanathan A, Deprez L, Zerka F, Danthine D, Frix AN, et al. A review in radiomics: making personalized medicine a reality via routine imaging. Med Res Rev. 2022; 42: 426-40.

218. Kickingereder P, Burth S, Wick A, Götz M, Eidel O, Schlemmer HP, et al. Radiomic profiling of glioblastoma: identifying an imaging predictor of patient survival with improved performance over established clinical and radiologic risk models. Radiology. 2016; 280: 880-9.

219. Kickingereder P, Götz M, Muschelli J, Wick A, Neuberger U, Shinohara RT, et al. Large-scale radiomic profiling of recurrent glioblastoma identifies an imaging predictor for stratifying anti-angiogenic treatment response. Clin Cancer Res. 2016; 22: 5765-71.

220. Anagnostopoulos AK, Gaitanis A, Gkiozos I, Athanasiadis EI, Chatziioannou SN, Syrigos KN, et al. Radiomics/radiogenomics

in lung cancer: basic principles and initial clinical results. Cancers (Basel). 2022; 14: 1657.

221. Saxena S, Jena B, Gupta N, Das S, Sarmah D, Bhattacharya P, et al. Role of artificial intelligence in radiogenomics for cancers in the era of precision medicine. Cancers (Basel). 2022; 14: 2860.

222. Singh G, Manjila S, Sakla N, True A, Wardeh AH, Beig N, et al. Radiomics and radiogenomics in gliomas: a contemporary update. Br J Cancer. 2021; 125: 641-57.

223. Bitencourt A, Daimiel Naranjo I, Lo Gullo R, Rossi Saccarelli C, Pinker K. AI-enhanced breast imaging: where are we and where are we heading? Eur J Radiol. 2021; 142: 109882.

224. Cho HH, Kim CK, Park H. Overview of radiomics in prostate imaging and future directions. Br J Radiol. 2022; 95: 20210539.

225. Lohmann P, Franceschi E, Vollmuth P, Dhermain F, Weller M, Preusser M, et al. Radiomics in neuro-oncological clinical trials. Lancet Digit Health. 2022; 4: e841-9.

226. Forte GC, Altmayer S, Silva RF, Stefani MT, Libermann LL, Cavion CC, et al. Deep learning algorithms for diagnosis of lung cancer: a systematic review and meta-analysis. Cancers (Basel). 2022; 14: 3856.

227. Painuli D, Bhardwaj S, Köse U. Recent advancement in cancer diagnosis using machine learning and deep learning techniques: a comprehensive review. Comput Biol Med. 2022; 146: 105580.

228. Ford J, Dogan N, Young L, Yang F. Quantitative radiomics: impact of pulse sequence parameter selection on MRI-based textural features of the brain. Contrast Media Mol Imaging. 2018; 2018: 1729071.

229. Molina D, Pérez-Beteta J, Martínez-González A, Martino J, Velasquez C, Arana E, et al. Lack of robustness of textural measures obtained from 3D brain tumor MRIs impose a need for standardization. PLoS One. 2017; 12: e0178843.

230. Zwanenburg A, Vallières M, Abdalah MA, Aerts HJWL, Andrearczyk V, Apte A, et al. The image biomarker standardization initiative: standardized quantitative radiomics for high-throughput image-based phenotyping. Radiology. 2020; 295: 328-38.

231. Clark K, Vendt B, Smith K, Freymann J, Kirby J, Koppel P, et al. The Cancer Imaging Archive (TCIA): maintaining and operating a public information repository. J Digit Imaging. 2013; 26: 1045-57.

232. Tomaszewski MR, Gillies RJ. The biological meaning of radiomic features. Radiology. 2021; 298: 505-16.

233. Brunet J, Walsh CL, Wagner WL, Bellier A, Werlein C, Marussi S, et al. Preparation of large biological samples for high-resolution, hierarchical, multi-modal imaging. bioRxiv. 2022. doi: 10.1101/2022.07.02.498430.